NSSI Neutron Newsletter

Number 4
December 2023

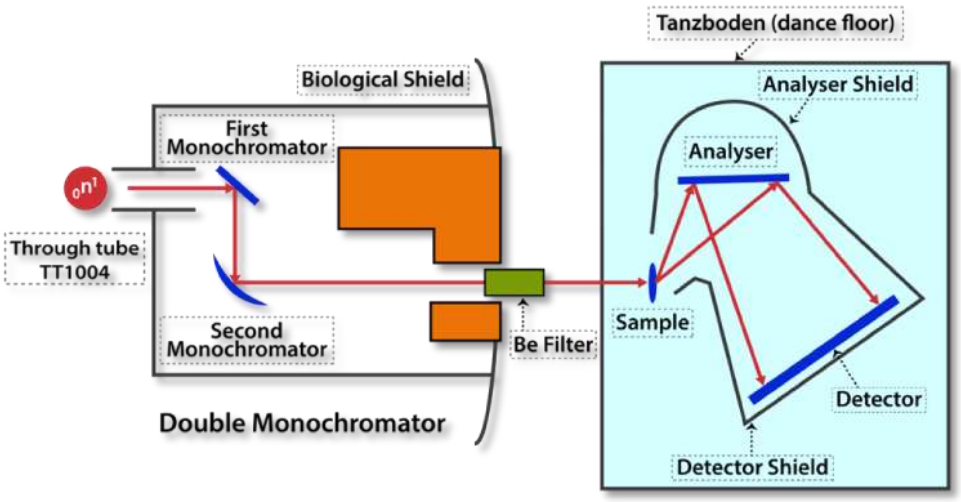

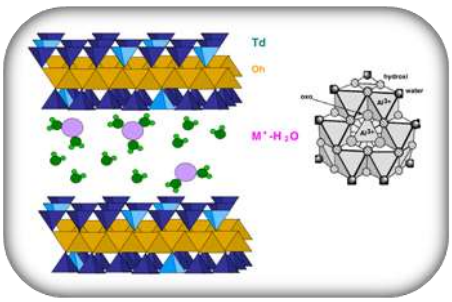

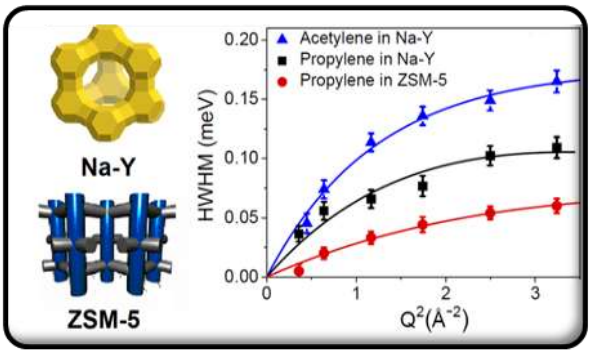

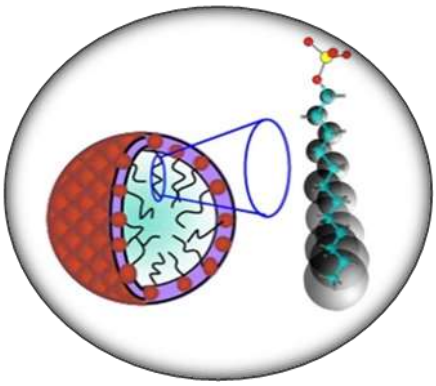

Neutron Scattering Society of India

Neutron Scattering Society of India (NSSI) was formed in 2008 to provide a forum for neutron users for promoting neutron-based research and development activities including applications in the country. The NSSI is the adhering society representing the neutron users in India on the Asia-Oceania Neutron Scattering Association (AONSA), which is an affiliation of various neutron scattering societies in the Asia-Oceania region. NSSI happens to be one of the founder members of the AONSA along with the respective neutron societies from Japan, South Korea, Australia and Taiwan. At present NSSI has more than 300 registered members from various universities and institutions spread all over the country.

Cover Page

Schematic and photograph of QENS spectrometer at Dhruva reactor (top) and schematics of range of systems (e.g. clay, zeolite and surfactant micelles) for which molecular motions have been studied using QENS (bottom). See the article on *Probing Stochastic Dynamics in Condensed Matter: Insights from Quasielastic Neutron Scattering Facility in India* by V.K. Sharma, H. Srinivasan and S. Mitra (page 16).

Contents

- Editorial 4
- Message from the President, NSSI 5
- Highlights of Neutron Research 6-15
- A short status review on Quasielastic Neutron Scattering Facility in India 16-38
- Links to forthcoming Neutron Conferences and Workshops 39-40
- NSSI application for membership 41

Editorial

Happy New Year 2024!

We are glad to bring out this fourth issue of the NSSI Newsletter. This issue contains highlights of a broad variety of high-quality neutron science done in India, covering both fundamental and applied aspects. The research areas include nanoparticle interactions, Li/Na battery materials, magnetism in different compounds and multilayers, and materials science. These highlights also emphasize the breadth of the neutron scattering techniques being pursued by the scientists in India.

This issue includes a topical review on quasi-elastic neutron scattering. The first part of the article has a description of the technique as implemented at the Dhruva reactor, followed by a review of the stochastic dynamics research at BARC over last 25 years. It is worth noting that the quasi-elastic neutron scattering research of stochastic dynamics has been pursued in India over last 5 decades, starting at the CIRUS reactor at BARC, Trombay.

We hope the readers will like this issue and contribute excellent highlights of their research to the future issues.

Editor: S. L. Chaplot

Managing Editor: V. K. Aswal (General Secretary, NSSI)

The NSSI Managing Committee:

Prof. Dhananjai Pandey, IIT BHU (President)

Prof. Ranjan Mittal, BARC & HBNI (Vice President, HQ)

Prof. K. G. Suresh, IITB (Vice President)

Prof. V. K. Aswal, BARC & HBNI (General Secretary)

Dr. P. D. Babu, UGC-DAE CSR (Treasurer)

Prof. A. Thamizhavel, TIFR (Member)

Prof. S. L. Chaplot, BARC & HBNI (Member)

Prof. S. M. Yusuf, BARC & HBNI (Member)

Prof. P. U. Sastry, BARC & HBNI (Member)

Published by The General Secretary, NSSI.

Copyright @The Neutron Scattering Society of India

Permission is given for reproducing a part of the contents of this Newsletter with acknowledgment of the Copyright holder.

Message from the President, NSSI

I am very happy to present the fourth issue of NSSI Newsletter (Dec 2023 issue) and wish to congratulate the Editors for maintaining its regularity and the high standard of selected highlights and the status report cum review article.

As with the past issues, the present issue of the Newsletter gives glimpse of high-quality neutron beam research on diverse range of phenomena/materials being carried out using primarily the facilities at the Dhruva reactor. These results are published in leading journals like Langmuir, Soft Matter, Phys Rev Mater, Phys Rev B, JMMM, J Mater Chem A, ACS Appl Electronic Mater and Structural Chem. One of the notable features of some of these researches is the insight provided by ab-initio MD simulations, including machine learned simulations, in interpreting the experimental observations. The topics covered in these highlighted publications range from soft matter to Li/Na ion battery materials, multilayers, lattice excitations, magnetism and structural chemistry. These highlighted articles are followed by a Status Review on QENS facility at Dhruva and a few significant findings resulting from this facility. I compliment all the contributors for their high-quality input to the Newsletter.

Last but not the least. The present membership of NSSI is a little over 300. I believe that this does not reflect the entire community of researchers in India who use neutrons as a probe for investigating whole range of phenomena in condensed matter, materials physics, materials chemistry and structural biology. I appeal to all the existing members of the NSSI to induct new members who are already using neutrons as a probe in their researches.

Dhananjai Pandey
President, NSSI

Highlights of Neutron Research

Amphiphilic Interaction Mediated Decoration on Pickering Emulsion Droplet

Stabilization of an oil phase is crucial for numerous industrial processes, and it demands a proper balance of complex interactions in an emulsion system. In Pickering emulsions, it is achieved by addition of nano particles. These nanoparticles get organized at the oil-water interface. The influence of interparticle interactions towards formation of stable emulsion and ordering of the stabilizing nanoparticles is intriguing and needs attention. In this work [1], the role of amphiphilic interactions between hydrophilic silica nanoparticles and F127 tri-block co-polymer towards the spontaneous formation of fairly stable Pickering emulsion has been studied using small-angle scattering. Unlike the usual random arrangements of the nanoparticles in conventional Pickering emulsion, a highly organized structure of the silica nanoparticles at the oil-water interface was observed (as manifested by SAXS correlation peak~ 0.2 nm^{-1}). The established standard Raspberry structural model of Pickering emulsion failed to explain such strong ordering as observed in the present case. MSANS data from Dhruva confirmed low-Q increase in scattering intensity owing to the formation of droplets. A plausible mechanism of formation of such special Pickering emulsion having high on-surface silica correlation is elucidated on the basis of combined interactions of block co-polymer and silica particles. A computer model is developed to elucidate the effects of size and distribution of the surface-decorating nanoparticles and their positional correlation.

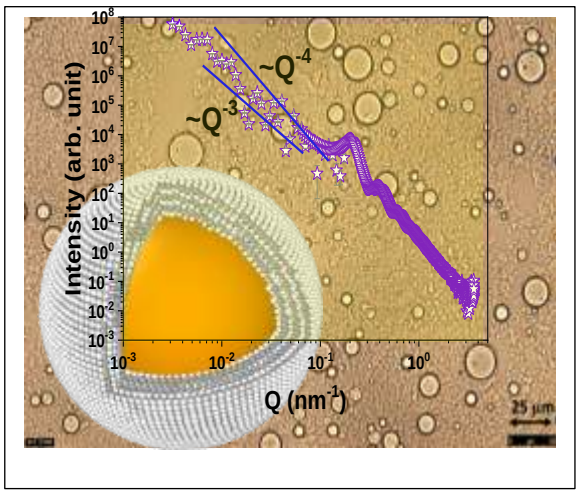

Confocal microscopy image of Pickering emulsion droplets. The inset shows the small-angle scattering profile over nearly 3 decades in wave-vector transfer (Q). Computer generated assembled structure for calculation of correlation is also depicted.

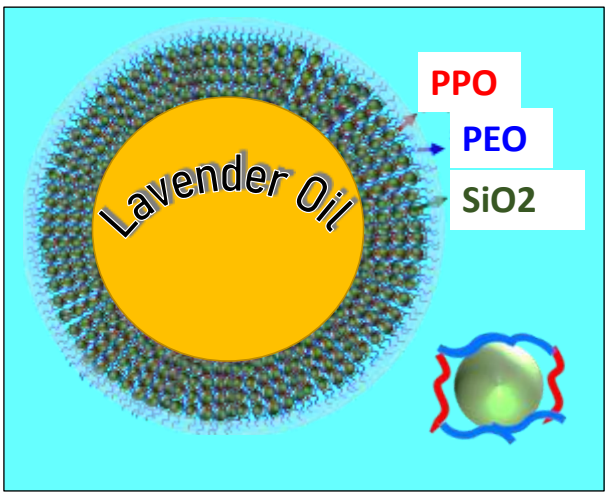

Schematic diagram illustrating the structure of silica-F127-Lavender oil Pickering emulsion droplet. The delicate balance between contrasting amphiphilic interactions among the PEO and PPO blocks of the block co-polymer unimers with Lavender oil and silica nanoparticles lead to strong correlation at droplet surface.

1. *Amphiphilic interaction-mediated ordering of nanoparticles in Pickering emulsion droplets*, D. Sen, A. Das, A. Kumar, J. Bahadur, R. K. Chaurasia, A. Khan, R. Ganguly, Soft Matter 19, 3953 (2023).

Contributed by D. Sen, BARC, Mumbai (email: debasis@barc.gov.in)

Understanding Thermo-responsive Liquid-liquid Phase Separation and associated Re-entrant Behavior in Nanoparticle-pluronic System

The complex interplay of DLVO and non-DLVO (e.g., steric, hydration, depletion, hydrophobic etc.) interactions in colloids gives rise to the emergences of intriguing re-entrant phase behavior. In re-entrant phase behavior, the system undergoes a phase change and return to original phase with respect to a monotonic variation in a specific physicochemical parameter. Such phase behavior is beyond the generalized understanding of colloidal science and has been observed in a variety of colloids (e.g., nanoparticles, protein, DNA) including nanoparticle-polymer system. However, in each of these cases, the underlying mechanism is different and involves more delicate multi-body interactions.

Recently, we have observed re-entrant liquid-liquid phase separation in silica nanoparticles-pluronic (triblock copolymer, P123) suspension, where the system transforms from stable one-phase to two-phase (aggregate) and then return back to original phase on increasing temperature [1]. The observed phase transition is reversible as well as thermo-responsive in nature, associated with lower consolute temperatures. The phase behaviour has been established using optical transmission and dynamic light scattering (Figures 1a) measurements. The pluronics are known to adsorb on the silica nanoparticles via forming the hydrogen bonding between ether oxygen of the ethylene oxide group and the OH group on the nanoparticle surface. The initial liquid-liquid phase separation and corresponding re-entrant at higher temperature are believed to be driven by temperature induced-changes in the hydrophobicity of this adsorbed layer of the P123.

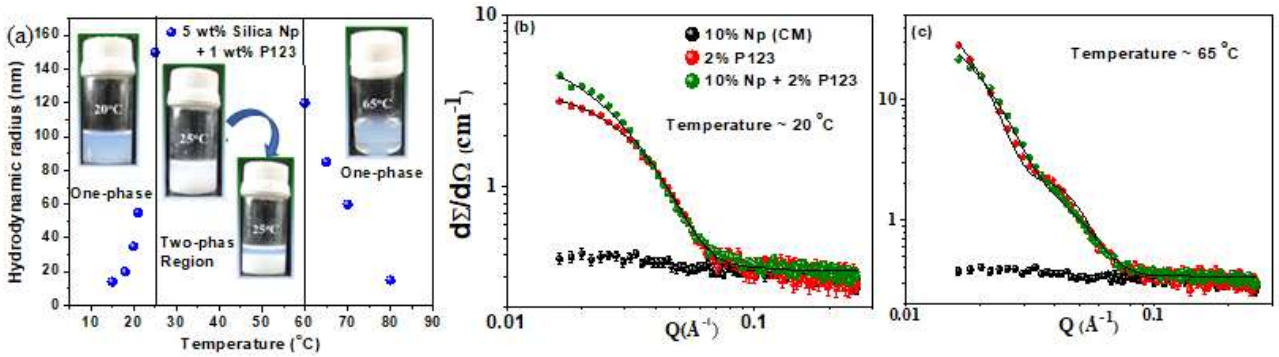

Fig. 1*. (a) Evolution of hydrodynamic size of 5 wt% silica nanoparticles (5 wt%, size ~ 27.0 nm) with 2 wt% P123 pluronic as a function of temperature. Inset photos show physical state of the suspension at respective temperatures. SANS data of 10wt% nanoparticles suspension in presence of 2 wt% P123, where nanoparticles are contrast-matched to the solvent are shown in (b) at 20 °C and (c) at 65 °C.*

The evolution of the interactions in nanoparticle-pluronic system is examined by small-angle neutron scattering (SANS). The SANS data of 10wt% nanoparticles + 2 wt% P123 suspension in nanoparticle contrast-matched condition at temperatures in initial (20 °C) and re-entrant (65 °C) are shown in Figures (b) and (c). At lower temperature, the pluronic micelles are found more attractive in presence of nanoparticles than those in the pristine P123 solution, suggesting that this attraction among adsorbed micelles are driving the initial liquid-liquid phase separation in the system. Interestingly, SANS data of mixed sample at higher temperature (65 °C) show almost similar scattering features to that of pure 2 wt. % P123 (measured in same solvent) (figure 1c). This temperature being above the cloud point of P123 solution, the pluronic aggregates are expected to be highly hydrophobic, leading to weakening of their interaction with nanoparticles. This suggests that the observed re-entrant behavior could be arising due to detachment of pluronic micelles from the nanoparticle surface with increase in temperature.

1. *Pluronic Induced Interparticle Attraction and Re-entrant Liquid–Liquid Phase Separation in Charged Silica Nanoparticle Suspensions,* S. Kumar, R. Ganguly, S. Nath, V. K. Aswal, Langmuir **39**, 8109 (2023).

Contributed by Rajib Ganguly, BARC, Mumbai (email: rajibg@barc.gov.in)

Intertwined Crystal Structure and Electrical Properties in Layered Battery Materials A_2Ni_2TeO6 (A = Na/Li): An Insight from Neutron Diffraction

Layered transition metal oxide compounds with intermediate layers of alkali ions (Li/Na) are of special important for battery applications as they show high ionic conductivity, high energy density, low dissipation energy, and improved alkali ion intercalation/deintercalation functionality due to their lamellar structure. Here, we report temperature evolution of the crystal structure and electrical properties, and their interconnection in the promising two-dimensional (2D) layered battery materials $A_2Ni_2TeO_6$ (A = Na/Li) by comprehensive neutron diffraction, Raman spectroscopy, and impedance spectroscopy studies [1]. We reveal that the crystal structures of Na- and Li-based compounds, with space group $P6_3/mcm$ and $Cmca$, respectively, have identical global crystal structures with alternating $(Ni/Te)O_6$ and alkali metal layers but with different internal structures of the alkali metal layers [Figs. (a-d)]. Despite the Li ion having smaller size and lighter weight than that of the Na ion, our results reveal that the Na compound has higher ionic conductivity than the Li compound [Fig. (g)]. By detailed crystal structural analysis, we divulge that the differences in the internal structures of the alkali metal ion layers, such as distance between the alkali metal ions, local crystal structural environment, and the relative site occupancies of the alkali metal ions, result in differences in the ionic conductivity. We have illustrated the Na/Li-ionic conduction pathways by soft bond valence sum analysis of the neutron diffraction patterns which reveal they are within the 2D planes of the alkali metal layers for both compounds [Fig. (c-d)]. Additionally, in this paper, we demonstrate a correlation between crystal structure and electrical properties, where anomalies are found for both temperature-dependent electrical and local crystal structural parameters at ~550K and ~250K for Na- and Li-based compounds, respectively [Figs (e-i)]. The present report facilitates an in-depth understanding of the microscopic crystal structure, electrical properties, and their inter-correlations which are essential for the design and fabrication of highly efficient layered battery materials.

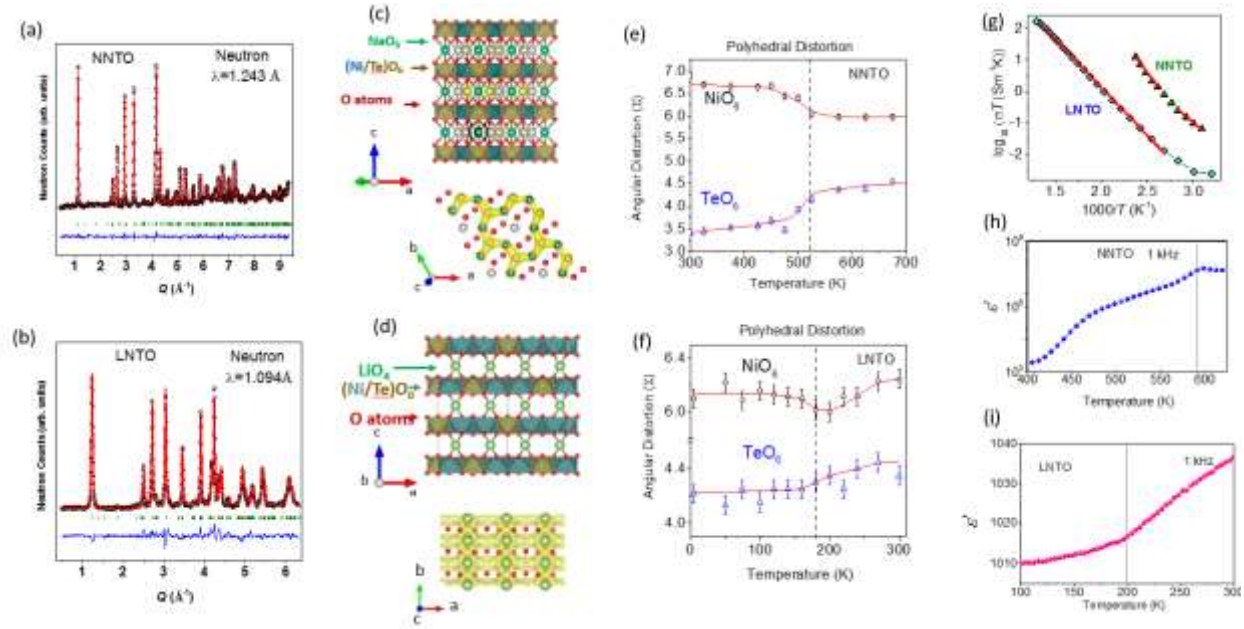

Figure. *The observed (circles) and simulated (red lines) neutron diffraction patterns for $A_2Ni_2TeO_6$ with (a) A=Na and (b) A=Li. The schematic layered crystal structure and in-plane ionic conduction pathways of $A_2Ni_2TeO_6$ with (c) A=Na and (d) A=Li. The temperature dependent Octahedral distortions for $A_2Ni_2TeO_6$ with (e) A=Na and (f) A=Li. Solid lines are guides to the eye. (g) The temperature dependent ionic conductions. The temperature dependent dielectric constant for $A_2Ni_2TeO_6$ with (h) A=Na and (i) A=Li.*

1. *Intertwined crystal structure and electrical properties in layered battery materials $A_2Ni_2TeO_6$ (A = Na/Li),* B. Saha, A. K. Bera, S. Kesari, and S. M. Yusuf, Phys. Rev. Mater. **7**, 085001 (2023).

Contributed by: A.K. Bera, BARC, Mumbai (*email: akbera@barc.gov.in*)

Li-ion Conduction Mechanism and its Pathways in Sorosilicate Compound $Li_2Cu_5Si_4O_{14}$: A Neutron Diffraction Study

The advancement of energy production and storage devices is currently a pressing issue for the community to achieve net zero-carbon emissions. In this context, rechargeable Li-ion batteries have emerged as the best choice among all the energy storage devices available in the market. In general, an all-solid-state battery (ASSB) (comprises of solid cathode, solid anode, and solid electrolyte) is of special interest. Understanding the microscopic conduction mechanism is a key requirement for designing high-performance solid Li-ion electrolyte materials for ASSB. In the recent past, researchers worldwide have extensively studied various transition metal-based solid Li-ion electrolyte materials to meet these criteria. With this keen interest, in this study, comprehensive ionic conduction properties of promising material $Li_2Cu_5Si_4O_{14}$ have been investigated by electrochemical impedance spectroscopy (EIS); and the microscopic conduction pathways are illustrated by neutron powder diffraction (NPD) [1]. The soft bond valence sum (BVS) analysis of room temperature NPD data has been performed to obtain the ionic conduction pathways within the unit cell.

Impedance data reveal a non-Debye type barrier hopping conduction mechanism (depressed semicircle in Cole-Cole plot; $-Z''$ vs. Z' [Fig. (a)]) with an activation energy of 1.25(4) eV [Fig. (b)]. The frequency dependence of ac-conductivity at a given temperature is well explained by the Jonscher's power law [Fig. (c)] and reveals a correlated barrier hopping mechanism of ionic conduction. The bond valence landscape (BVL) map [Fig. (e)] has been determined from BVS analysis of neutron diffraction patterns [Fig. (d)], reveals three-dimensional Li conduction. Four effective Li-ion conduction channels (A, B, C, and D) are identified. However, there are bottlenecks in the conduction channels, especially in A and D, which are responsible for the observed high value of activation energy. This study provides an in-depth understanding of Li-ionic conduction mechanism and root cause for high value of activation energy. Such understandings are useful for the design of high efficient battery materials.

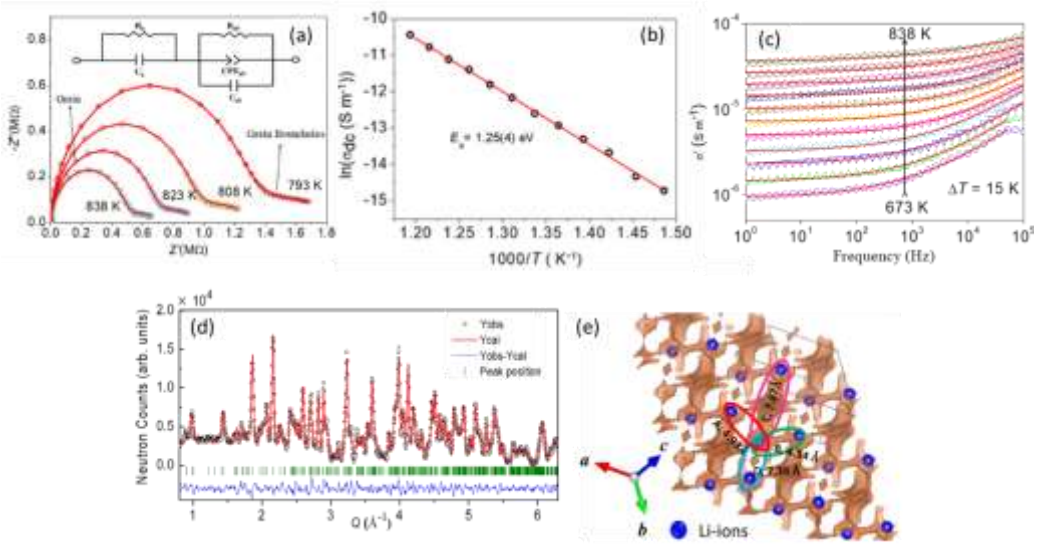

Figure. *(a) The Cole-Cole plots of impedance (-Z″ vs. Z′) for LCSO. (b) Inverse temperature dependence of total dc conductivity (σ_{dc}) (Arrhenius plot). (c) Frequency dependence of real part of ac conductivity σ′ for LCSO. (d) The NPD pattern of $Li_2Cu_5Si_4O_{14}$ [experimental (black circle), calculated (red line) and difference patterns (blue line)]. (e) The conduction pathways for lithium ions determined by the soft BVS analysis of NPD pattern.*

1. *Li-ion Conduction Mechanism and Relaxation Dynamics in Sorosilicate Compound $Li_2Cu_5(Si_2O_7)_2$*, K. S. Chikara, A. K. Bera, A. Kumar, S. M. Yusuf, ACS Applied Electronic Materials, **5**, 5137 (2023).

Contributed by: A.K. Bera, BARC, Mumbai (*email: akbera@barc.gov.in*)

Topology Driven and Soft Phonon Mode Enabled Na-ion Diffusion in Quaternary Chalcogenides, Na_3ZnGaX_4 (X=S, and Se)

We identify that the specific topology of Na zig-zag chains in Na_3ZnGaX_4 (X=S, Se) provides the low-barrier energy pathways for Na-ion diffusion [1]. Using inelastic neutron scattering (INS), quasielastic neutron scattering (QENS), and ab-initio molecular dynamics (AIMD) simulations, we bring out the role of specific zig-zag Na chains topology in the framework structure and its dynamics, leading to Na diffusion. The unique insights obtained from these experiments and simulations enable us to investigate the Na- diffusion at microscopic level. The INS result shows the presence of strongly anharmonic phonons at elevated temperatures. The harmonic phonon eigenvector calculation shows that low-energy phonon modes involve high amplitude of vibration of Na at 32*g* sites. The QENS measurements in the Na_3ZnGaX_4 (X=S, Se) show significant quasielastic broadening at elevated temperature, which indicates presence of fast Na-ion dynamics. The calculated phonon density of states using AIMD also reveals that Na at 32*g* Wyckoff sites has sufficiently shallow potential, which facilitates diffusion. The calculated Na occupation probability in ab-plane is shown in Fig. 1, which reveals the large participation of Na from 32*g* sites in diffusion.

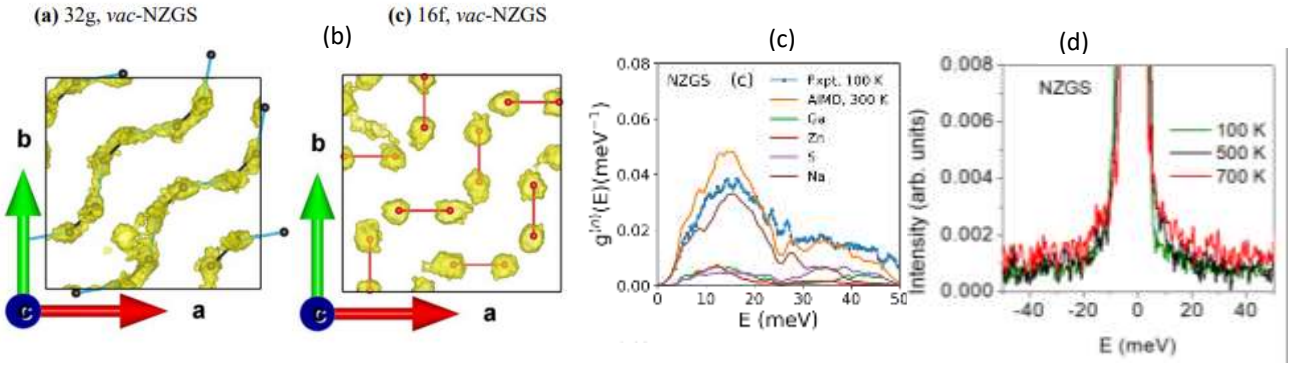

Fig 1: (a-b) The Na-ion trajectory located at 32g and 16f Wyckoff sites in Na_3ZnGaS_4 and (c) measured and calculated neutron weighted phonon density of states in Na_3ZnGaS_4. (d) Temperature dependence of quasielastic spectra of Na_3ZnGaS_4

These findings on the role of specific Na zig-zag topology in Na-diffusion may offer new possibilities for exploring novel transport properties, which leads to a better understanding of the microscopic aspects of Na^+ diffusion and provides vital information for designing solid electrolytes.

1. *Topology Driven and Soft Phonon Mode Enabled Na-ion Diffusion in Quaternary Chalcogenides, Na_3ZnGaX_4 (X=S, and Se),* Sajan Kumar, M. K. Gupta, R. Mittal, S. Sundaramoorthy, A. Choudhury, N. C. Osti, A. I. Kolesnikov, M. B. Stone, Y.Cheng, and S. L. Chaplot; Journal of Materials Chemistry A **11,** 23940 (2023).

Contributed by R. Mittal, BARC, Mumbai (email: rmittal@barc.gov.in)

In-field neutron diffraction study on $Na_5Co_{15.5}Te_6O_{36}$

Structural, magnetic and dielectric properties of $Na_5Co_{15.5}Te_6O_{36}$ have been studied which exhibited short range magnetic correlation and dielectric anomaly in the system above Neel temperature (50K) [1]. Analysis of temperature dependent neutron diffraction study carried out at powder diffractometer (PD-3) reveal that the canted spin orientation is responsible for antiferromagnetic ordering. This also exhibited partially occupied Co site from other Co site give rise to short range correlation of ferromagnetic and antiferromagnetic nature. Aforementioned additional characterization like dielectric, magnetization, electron-spin resonance suggested existence of short-range magnetic correlation. The step like behaviour in isothermal magnetization suggested metamagnetic transition in the compound.

In order to understand these, neutron diffraction study under the magnetic field have been carried out and effect of magnetic field could be observed in the form of modification in peak corresponding to magnetic order.

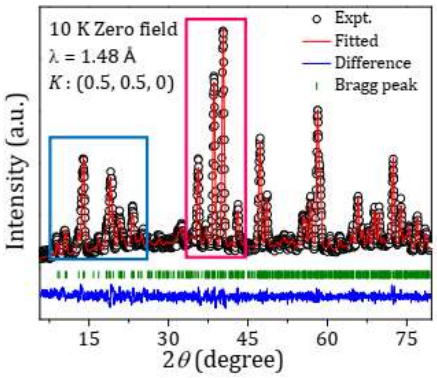

Rietveld refined ND pattern of $Na_5Co_{15.5}Te_6O_{36}$ at 10K.

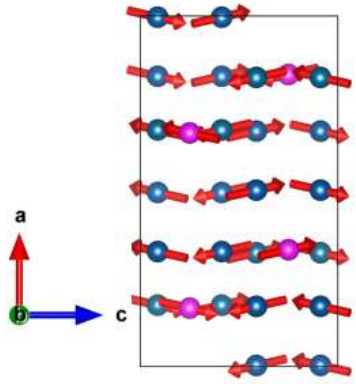

Antiferromagnetic canted spin arrangement

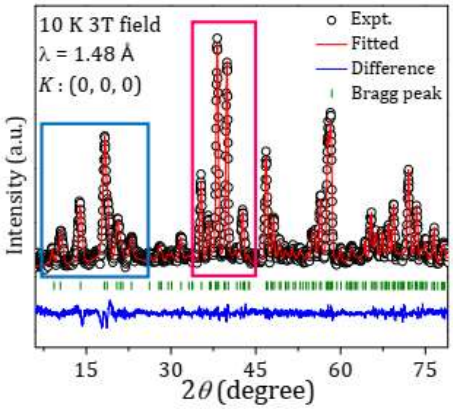

Rietveld refined ND pattern of $Na_5Co_{15.5}Te_6O_{36}$ at 10 K with 3 T magnetic field.

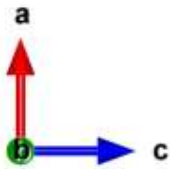

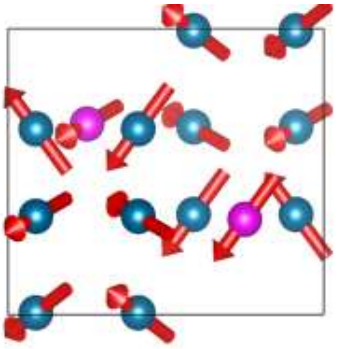

Modified spin structure indicating the effect of magnetic field

Analysis of magnetic-field-dependent neutron diffraction confirmed off centering of Co spins with applied magnetic field. This affirm that spin flop transition with increase in magnetic field drive to metamagnetic phase transition.

1. *Short-range magnetic correlation, metamagnetism, and coincident dielectric anomaly in Na5Co15.*5Te6O36, R. A. Saha, J.Sannigrahi, I. Carlomagno, S.D. Kaushik, Carlo Meneghini, Mitsuru Itoh, V. Siruguri, Sugata Ray, Phys. Rev. B, **107**, 155105 (2023*)*

Contributed by S.D. Kaushik, UGC-DAE CSR, Mumbai (email: sdkaushik@csr.res.in)

Emerging Interfacial Magnetization in all Ferromagnetic and Isovalent Manganite Heterostructures

The emergent interfacial phenomena in transition metal perovskite oxide (ABO_3) heterostructures are induced by the strong coupling between spin, orbital, charge and lattice degrees of freedom. The BO_6 oxygen octahedra, which are intimately correlated to orbital, charge and spin order in perovskite oxides, enable the structural distortion by decreasing the B-O-B bond angles (β) and increasing the B-O bond lengths (d), which leads to directly change the electronic and magnetic properties. In addition, ABO_3 heterostructures offer an exceptional means to tune the lattice structure, where the oxygen octahedral rotation can be regulated either by interfacial strain or by interfacial oxygen octahedral coupling (OOC) for enhancing the exchange interaction and magnetization at the interfaces. Combining depth-dependent magnetic characterization technique; (polarized neutron reflectivity, PNR); and theoretical calculation (density functional theory), we investigated interface-driven magnetic exchange interactions due to a modification in the octahedral rotations at the interfaces in an isovalent $La_{0.67}Ca_{0.33}MnO_3$ (LCMO)/$La_{0.67}Sr_{0.33}MnO_3$ (LSMO) multilayer [1]. Figure (a) shows the schematic and scanning transmission electron microscopy image of the multilayer. The energy dispersive x-ray spectroscopy (EDS) measurements were performed to distinguish the LCMO and LSMO layers. The elemental maps determined from characteristic La-$L_{\alpha1}$, O-$K_{\alpha1}$, Mn-$K_{\alpha1}$, Ca-$K_{\alpha1}$ and Sr-$K_{\alpha1}$ EDS edges from the multilayer are shown in Figs. 1(b) and (c), suggesting high-quality layer structure. Figure 1(d) shows the PNR data at different temperature revealing the detail structure and magnetic depth profiles shown in Fig. 1 € and (f). PNR results determined a length scale of ~ 8 unit cells at the interface, which demonstrated a modification in magnetic properties. PNR results suggested existence of an ultrathin FM interfacial LCMO layer at LSMO/LCMO (LSMO grown on LCMO) interface and the absence of such interfacial ferromagnetism at LCMO/LSMO (LCMO grown on LSMO) interface at 200 K, which is well above the transition temperature of LCMO. The results also predicted a low-temperature exchange bias for these all ferromagnetic based multilayers. The first principle calculations showed that asymmetric magnetization at interfaces are due to the different magnitude of nearest-neighbour exchange interactions as a result of interface-driven deformation of oxygen octahedral at the interfaces.

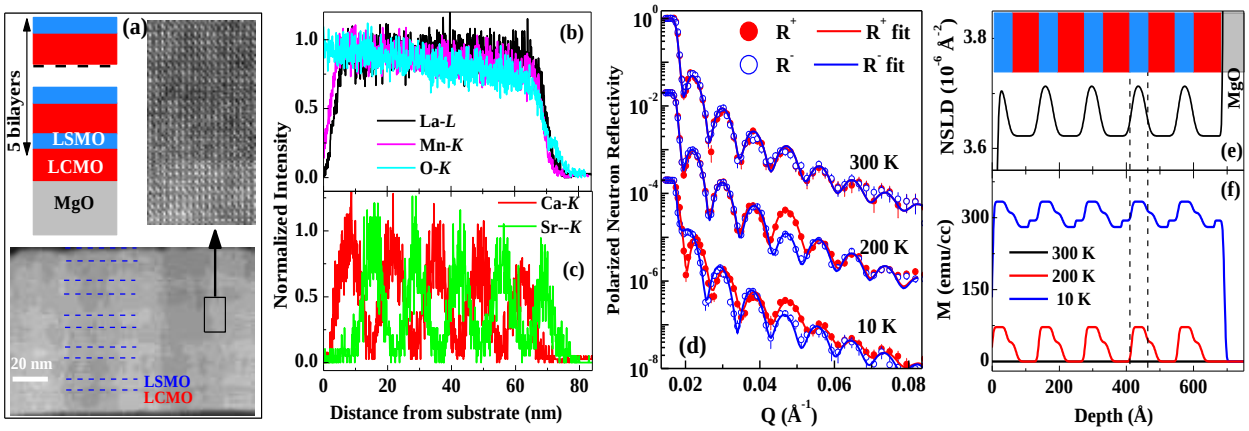

Figure (a) Schematic and STEM image of LSMO/LCMO multilayer. (b and c) The depth profiling of the concentration of different elements in the multilayer obtained from EDS measurements. (d) PNR measurements at different temperatures. Nuclear scattering length density (e) and magnetization (f) depth profiles of multilayer at different temperature obtained from PNR data.

1. *Emerging interfacial magnetization in isovalent manganite heterostructures driven by octahedral coupling*, Y. Kumar, H. Bhatt, S. Kakkar, C.J. Kinane, A. Caruana, S. Langridge, C. Bera, S. Basu, M. A. Roldan, and S. Singh, Phys. Rev. B **108**, 174410 (2023).

Contributed by S. Singh, BARC, Mumbai (email: surendra@barc.gov.in)

Low-temperature Ordering in Fe/Rh and Fe(N)/Rh Multilayers

The bulk FeRh alloy in B2-order phase near equiatomic composition undergoes a first-order phase transition from a low temperature α″- antiferromagnetic (AFM) state to a high temperature α′- ferromagnetic (FM) state around a transition temperature (T_t) of ~ 350 K. This transition (AFM to FM) is accompanied by a volume expansion of ~ 1% and depends on external parameters like Fe_xRh_{1-x} composition, concentration of doping element, strain and electric/magnetic fields etc. The FeRh alloy has shown promising results for possible application in magnetic recording media, antiferromagnet memory and low-power spintronics devices. In general, B2-ordered FeRh alloy thin films are grown by co-deposition using molecular beam epitaxy/sputtering technique at high temperature followed by post-annealing at temperature > 500 °C, which leads interdiffusion at interfaces and deteriorate the properties. However, low temperature annealing of a multilayer and a doped multilayer provide high quality alloy phase formation. We carried out systematic study of the evolution of FeRh alloy phase formation in Fe/Rh multilayers as a function of annealing temperature and nitrogen doping [1]. The schematic and PNR results for as-deposited and multilayer annealed at 300°C for Fe/Rh and FeN/Rh systems are shown in the upper and lower panel of Figure, respectively. The PNR results suggested formation of B2-ordered FeRh alloy phase at much lower annealing temperature of 300 °C and 400 °C for Fe/Rh and FeN/Rh multilayers, respectively. PNR results also predicted a variation in magnetization along the thickness of the multilayers annealed at these temperatures, which may be due to the uncompensated (remaining) Rh phase at different depths (Figure). PNR measurements for Fe/Rh multilayer annealed at 300 and 400 °C indicated that the alloy phase is ferromagnetic at RT with a reduced average MSLD of ~ 1.7×10^{-6} $Å^{-2}$. In contrast the FeN/Rh multilayer annealed at 300 °C showed intermixed interface layer with traces of FeN and Rh layers along the depth of the film. The reduced difference in spin-dependent PNR (i.e., low value of NSA) for FeN/Rh multilayer annealed at 300 °C further suggested a suppression of the FM phase indicating that the interfacial disordered phase is nonmagnetic.

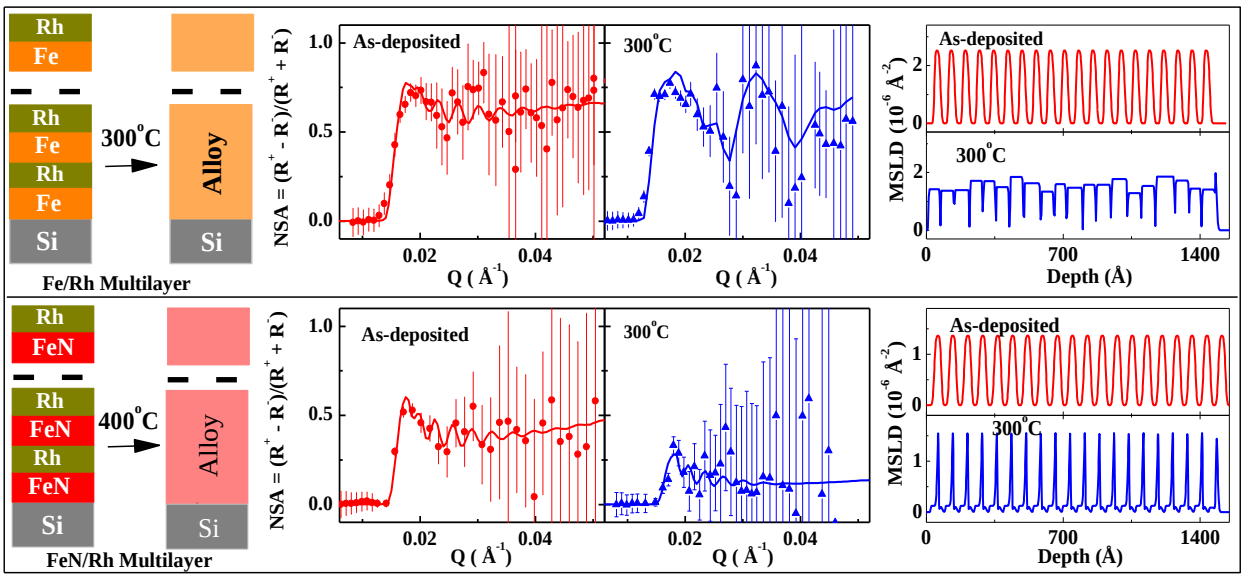

Figure: Schematic of multilayers before annealing and after annealing, PNR data and corresponding magnetization depth profiles for Fe/Rh (upper panel) and FeN/Rh (lower panel) systems.

1. *Formation of B2-ordered FeRh alloy thin films on annealing of pure and nitrogen doped Fe/Rh multilayers,* P. Negi, M. Gupta, R. Rawat, R. Joshi, H. Bhatt, Surendra Singh, V R Reddy and H. Kumar, Journal of Magnetism and Magnetic Materials, **581**, 170941 (2023).

Contributed by S. Singh, BARC, Mumbai (email: surendra@barc.gov.in)

Glycine Silver Nitrate and Effect of Deuteration

Glycine silver nitrate (GSN) is the first organometallic crystal of glycine with silver and nitrate, which showed ferroelectricity, and it undergoes displacive phase transition. Our earlier study on fully deuterated GSN(FDGSN) showed that the crystal structure changes on full deuteration showing isotopic polymorphism. In order to probe further the effect of deuteration, partially deuterated, C Deuterated GSN (CDGSN) and N deuterated GSN (NDGSN) crystals were grown. Repeated recrystallization was carried out to grow large size crystals. Attempt to study the crystal structure of deuterated crystals using single crystal neutron diffraction were not very successful as the large size crystals were twinned, hence single crystal x-ray diffraction was carried out to elucidated the structural details [1]. The crystal structure of C-deuterated was similar to FDGSN forming 2 dimensional polymeric structures extended along the c-axis, In CDGSN, the silver ion is mononuclear similar to that in FDGSN with no Ag-Ag coordination. N deuterated had crystal structure similar to that of GSN. The nitrate ion, the silver ion and zwitterionic glycine form a three-dimensional network unlike the case in CDGSN. The silver ion is binuclear with Ag-Ag coordination similar to that in GSN. In both crystal structures the silver ion has an oxidation state of +1. NDGSN and GSN have higher Ag···O interactions compared to that of CDGSN and FDGSN. NDGSN and GSN have Ag···Ag interaction, which is totally absent in CDGSN and FDGSN. Raman measurements showed the partial deuteration of the compounds. The C deuteration changes the coordination of the silver. In FDGSN and CDGSN, Ag ion coordinates to the hydrogen which is covalently bonded to carbon of zwitterionic glycine whereas in NDGSN and GSN this coordination of Ag ion with hydrogen is absent as shown in Fig. 1.

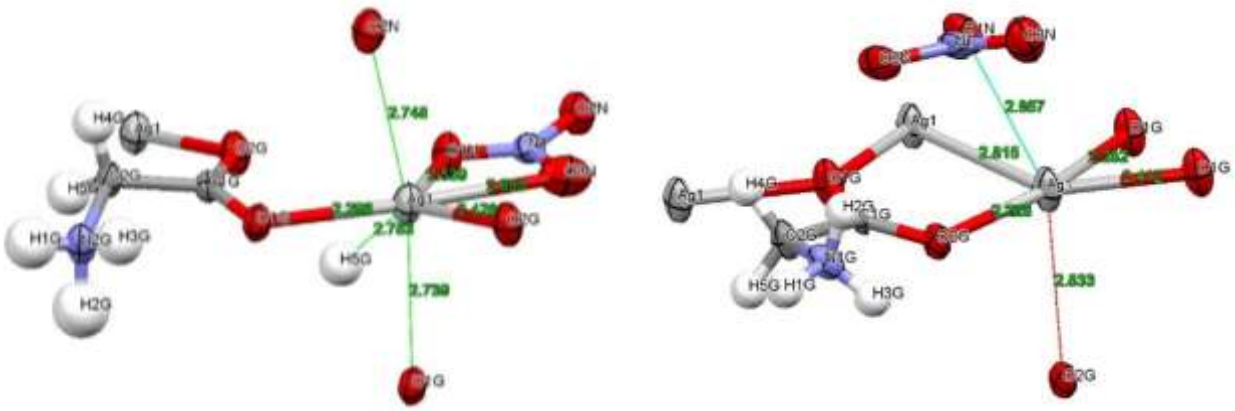

Figure 1. gives the coordination distances of silver in CDGSN and NDGSN respectively

1. *Effect of C deuteration in forming isotopic polymorph of glycine silver nitrate*, R. Chitra, R. R. Choudhury, Frederic Capet, Pascal Roussel, Himal Bhatt, Structural Chemistry, DOI:10.1007/s11224-023-02228-7 (2023)

Contributed by: R. Chitra, BARC, Mumbai (Email: rchitra@barc.gov.in)

Distinct Anharmonic Characteristics of Phonons driven Lattice Thermal Conductivity and Thermal Expansion in Bulk $MoSe_2$ and WSe_2

Phonons are the primary heat carrier in semiconductors and insulators, while phonon-phonon scattering limits heat conduction. These scattering rates are largely associated with the temperature dependence of phonon anharmonicity (explicit anharmonicity).

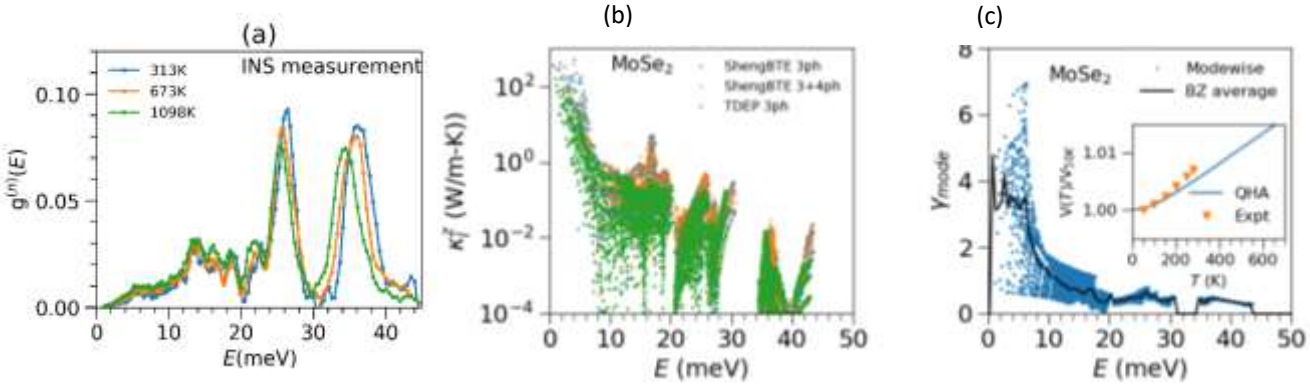

Figure1. (a) The temperature dependence of neutron weighted phonon density of states in MoSe2. (b) The calculated lattice thermal conductivity contributed from individual modes in $MoSe_2$ using different simulation schemes;(c) The calculated mode Grüneisen parameters using pressure dependence of phonon frequencies. The inset shows the fractional change in volume with temperature.

Using inelastic neutron scattering (INS) and X-ray diffraction measurements, together with ab-initio and machine-learned molecular dynamics simulations, we have investigated the anharmonic atomic dynamics, thermal transport and thermal expansion in bulk dichalcogenides $MoSe_2$ and WSe_2 [1]. We measured the temperature dependence of the phonon density of states (DOS) from 313 K to 1098 K using INS, which is used to benchmark our simulations and assess the strength of the anharmonicity. Our mode-resolved lattice-thermal conductivity calculation reveals that the major contribution (~ 90%) to total lattice thermal conductivity is attributed to the low-energy phonons. Thus, the less explicit anharmonic low-energy phonons contribute the significant thermal conductivity at ambient temperature. In contrast, the volume-dependent anharmonicity is quite large for low-energy phonons, which exhibit large positive Grüneisen parameters causing the large thermal expansion of the material. Hence, thermal transport and thermal expansion are attributed to distinct anharmonic characteristics of phonons and are primarily driven by low energy modes below ~20 meV.

1. *Distinct anharmonic characteristics of phonons driven lattice thermal conductivity and thermal expansion in bulk $MoSe_2$ and WSe_2,* M. K Gupta, Sajan Kumar, R. Mittal, S. K. Mishra, S. Rols, O. Delaire, A. Thamizhavel, P. U. Sastry, and S. L. Chaplot; Journal of Materials Chemistry A **11,** 21864 (2023)**.**

Contributed by R. Mittal, BARC, Mumbai (email: rmittal@barc.gov.in)

A short status review on a Neutron Technique

Probing Stochastic Dynamics in Condensed Matter: Insights from Quasielastic Neutron Scattering Facility in India

V. K. Sharma*, H. Srinivasan and S. Mitra[#]

Solid State Physics Division, Bhabha Atomic Research Centre, Mumbai 400085 India
&
Homi Bhabha National Institute, Anushaktinagar, Mumbai 400094, India

Email: *sharmavk@barc.gov.in; [#]smitra@barc.gov.in

Abstract

Quasielastic neutron scattering (QENS) technique is a powerful method for investigating stochastic dynamics in condensed matter. The article provides a concise overview of the fundamental principles of QENS technique and highlights the application of this technique in the study of diffusion mechanism in condensed matter. Emphasizing the capabilities of the QENS spectrometer installed at the Dhruva reactor in Trombay, this article delves into specific studies conducted on various systems including confined fluids in nanoscopic regimes (e.g., water filtration membranes, clays, or zeolites), liquid crystals, monolayer-protected nanosized metal clusters, self-assembled aggregates like micelles and liposomes, as well as investigations into complex fluids such as deep eutectic solvents and hydration gels. This comprehensive review highlights the pivotal role of QENS spectrometer at Dhruva, contributing to profound insights into diffusion mechanisms within condensed matter and fostering notable advancements in diverse scientific domains.

1. Introduction

The study of atomic and molecular dynamics in condensed matter is crucial for understanding material properties, and the advancement of novel, technologically important materials. Depending on the manner in which species move within material, dynamics can be categorized into two types: (i) periodic motion (e.g. lattice vibrations, etc) and (ii) stochastic motions (e.g. translational diffusion, molecular reorientation, etc). The exploration of periodic motions yields valuable insights into the phonon density of states, contributing to an enhanced understanding of thermal expansion behavior, phase transitions, and thermal transport properties. On the other hand, the investigation of stochastic dynamics unveils details about diffusion processes within the system, offering microscopic perspectives that elucidate the fundamental origins of macroscopic transport properties like viscosity and conductivity. Neutron scattering emerges as an exceptional experimental tool in this pursuit, particularly due to the close energy match between thermal neutrons and relevant excitations in condensed matter [1-4]. Moreover, the wavelength of thermal neutron matches with the order of interatomic distances, presenting a unique advantage. During an inelastic neutron scattering experiment, in which a finite amount of energy is exchanged between the neutron and the system, the scattered intensity is analysed with respect to both energy transfer (E) and wave vector transfer (Q). Thermal neutron can be used to study both periodic and stochastic dynamics occurring in the materials. Periodic motions manifest as inelastic peaks in the energy spectrum (Fig. 1(a)), reflecting characteristic frequencies, while thermally activated stochastic motions, encompassing diffusion and reorientation, contribute to the broadening of the elastic peak at zero energy transfer, known as quasielastic broadening as shown in Fig. 1(a). Quasi-elastic Neutron Scattering (QENS) technique is a method to study the stochastic dynamics in condensed matter [2-3]. In this method, spectra are generally measured centred at elastic line i.e. zero energy transfer within a limited energy transfer

range. Depending on the energy resolution of the spectrometer and available energy transfer range, QENS can probe dynamics of species on a very wide range of time scales spanning from nanoseconds to subpicoseconds. Being a scattering technique, QENS has a significant advantage over other complementary experimental techniques (e.g. NMR, fluorescence spectroscopy) due to an additional variable, wave vector transfer *Q*, which provides spatial information related to the geometry of the motion. QENS offers a unique possibility of analysing spatial information of atomic or molecular motions in their development over time.

The QENS technique provides both quantitative and qualitative insights into the molecular motion. Qualitatively, it unveils the geometrical mechanisms underlying the motion, while quantitatively, it provides information on correlation times and length scales associated with the dynamic processes. Moreover, the QENS method facilitates the determination of hindering potentials by exploring the temperature dependence of correlation times. In essence, QENS experiments encompass a comprehensive approach, enabling the extraction of key information about stochastic motion, including its time-scale, geometry, and the nature of hindering potentials. In particular, QENS is exceptionally well- suited for studying the dynamics of hydrogenous systems (such as proton, hydrogen gas, water, hydrocarbons, biological systems) because of the large scattering cross-section of the hydrogen compared to that of any other elements (σ_H ~ 81 barns, $\sigma_{\text{other elements}}$ ~ 4–5 barns). The substantial difference of scattering cross section between hydrogen and any other elements is evident as shown in Fig. 1(b). In contrast to X-rays, neutron scattering primarily emanates from the nucleus, leading to variations in scattering cross-sections for different isotopes. For comparison, the scattering cross-section for hydrogen and deuterium is also shown schematically in Fig. 1(b). It is evident that scattering cross section is exceptionally high for hydrogen compared to deuterium. This enables QENS to offer unique insights into the dynamic behavior of hydrogenous systems, leveraging the distinctive scattering properties of neutrons and their sensitivity to isotopic variations.

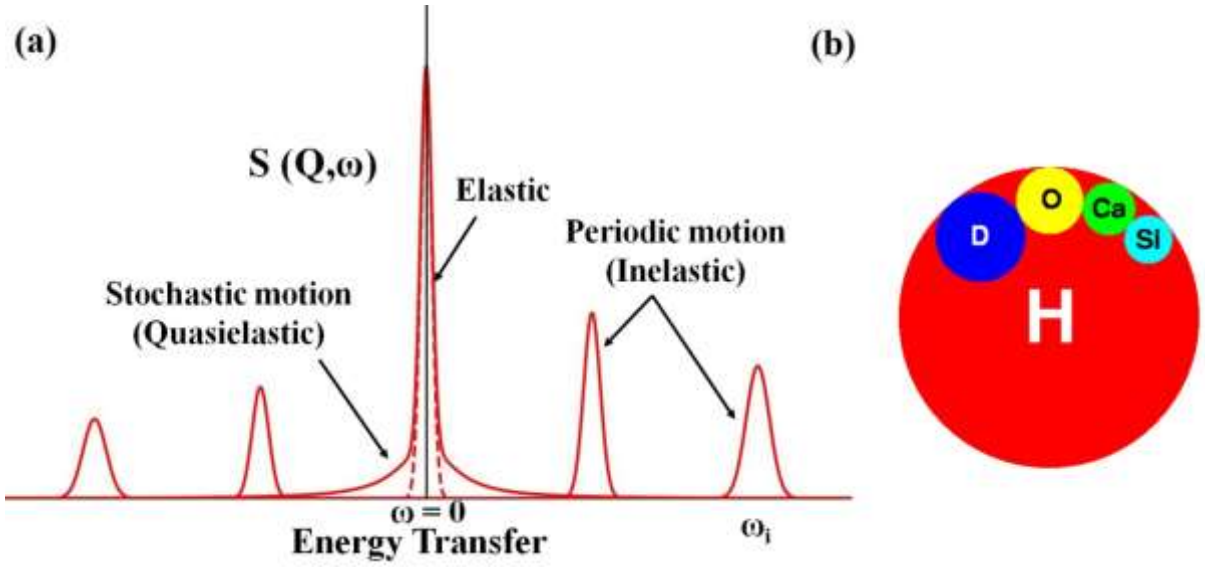

Fig. 1 (a) Schematic depiction of variation of dynamic structure factor *S* (*Q*,ω) with respect to energy transfer. Elastic, inelastic, and quasielastic components of neutron scattering spectrum are shown. The inelastic scattering has contributions from periodic motions manifesting at characteristic frequencies, while stochastic motions contribute to a broadening of the elastic line cantered at zero energy transfer. (b) Comparative representation of neutron scattering cross sections for various elements and isotopes, revealing the pronounced scattering potency of hydrogen for neutrons.

This review article is organised as follows. In the next section, a concise overview of the fundamental theoretical framework of QENS is given. In the subsequent section, details of the QENS spectrometer at Dhruva are discussed. In the next section, various examples showcasing the diverse range of systems studied using the QENS spectrometer at Dhruva will be discussed. These examples

encompass monolayer-protected metal clusters, liquid crystals, confined fluids in nanoscopic regimes, complex fluids, and self-assembled aggregates, offering a comprehensive understanding of the versatility and applicability of QENS. At the end, the concluding sections encapsulate a summary of key findings and culminate with a perspective on the overarching contributions and potential of QENS.

2. Basic Theoretical Framework of Quasielastic Neutron Scattering

In a QENS experiment, the scattered neutron intensity is measured as a function of both energy transfer ħω (= E_0-E, where E_0 and E are initial and final energies of neutrons) and wavevector transfer $\boldsymbol{Q}$ (= $\boldsymbol{k}_0$-$\boldsymbol{k}$, where $\boldsymbol{k}_0$ and $\boldsymbol{k}$ are initial and final wavevectors of the neutrons). The observed neutron intensity is associated with a double differential scattering cross-section $\frac{\partial^2\sigma}{\partial\boldsymbol{\Omega}\partial\omega}$ which gives the probability that a neutron with incident energy E_0, leaves the solid angle element $d\boldsymbol{\Omega}$, after scattering from the sample, about the direction $\boldsymbol{\Omega}$ and with an energy exchange between ħω=E-E_0 and ħ(ω+dω). The double differential scattering cross-section encompasses two distinct contributions arising from coherent and incoherent scattering interactions between the neutrons and the sample, and can be expressed as [2-3],

$$\frac{\partial^2\sigma}{\partial\boldsymbol{\Omega}\partial\omega} \propto \frac{k_f}{k_i}\left[\sigma_{coh}S_{coh}(\mathbf{Q},\omega)+\sigma_{inc}S_{inc}(\mathbf{Q},\omega)\right] \tag{1}$$

where, S_{coh} and S_{inc} are the coherent and incoherent scattering laws, σ_{coh} and σ_{inc} are the coherent and incoherent scattering cross sections; ħω is the energy transfer and $\boldsymbol{Q} = \boldsymbol{k_f} - \boldsymbol{k_i}$, is the momentum transfer resulting from the scattering process. The coherent scattering law $S_{coh}(\boldsymbol{Q},\omega)$ provides insights into pair-correlations within the system, whereas the incoherent component, $S_{inc}(\boldsymbol{Q},\omega)$ is specifically linked to the self-correlation function. In the case of hydrogenous samples, the scattered intensity will be dominated by the incoherent scattering from the hydrogen atoms in the sample, which is due to the exceptionally high incoherent scattering cross section of hydrogen ($\sigma_{inc}^{H} >> \sigma_{inc/coh}^{any\ atom}$). In which case, eq. (1) can be written as

$$\frac{\partial^2\sigma}{\partial\boldsymbol{\Omega}\partial\omega} \propto \frac{k_f}{k_i}\sigma_{inc}S_{inc}(\mathbf{Q},\omega) \tag{2}$$

The incoherent scattering law $S_{inc}(\mathbf{Q},\omega)$ can provide information about the diffusion mechanism of the system as it is related to the van-Hove self-correlation function, $G_s(\boldsymbol{r},t)$, through a space-time Fourier transform,

$$S_{inc}(\mathbf{Q},\omega) = \int_{-\infty}^{\infty} dt \int d^3r e^{-i(\omega t - \mathbf{Q}.\mathbf{r})} G_s\left(\mathbf{r},t\right) \tag{3}$$

$G_s(\boldsymbol{r},t)$ provides the probability of finding a particle at a point $\boldsymbol{r}$ in space after a time t, given the particle started at the origin at t = 0. Therefore, based on eq. (2) and (3), it is clear that the measured QENS spectra can provide information about self diffusion of the species.

It is interesting to study the behaviour of the $G_s(\boldsymbol{r},t)$ in the long time limit $t\to\infty$. Hence, $G_s(\boldsymbol{r},t)$ can be written as a sum of two parts as

$$G_s(\mathbf{r},t) = G_s(\mathbf{r},\infty) + G'_s(\mathbf{r},t) \tag{4}$$

where the first term is independent of time whereas the second term is time dependent part. One can obtain the corresponding incoherent intermediate scattering function (IISF) by taking spatial Fourier transform of Eq (4) and can be expressed as

$$I_{inc}(\mathbf{Q},t) = I_{inc}(\mathbf{Q},\infty) + I_{inc}(\mathbf{Q},t) \tag{5}$$

The corresponding incoherent scattering law can be obtained by taking temporal Fourier transform and can be written as

$$S_{inc}(\mathbf{Q},\omega) = I_{inc}(\mathbf{Q},\infty)\delta(\omega) + S_{inc}'(\mathbf{Q},\omega) \tag{6}$$

The $S_{inc}(\mathbf{Q},\omega)$ has been separated into purely elastic component, $I_{inc}(\mathbf{Q},\infty)\delta(\omega)$, and another one called quasielastic term which possesses a non-vanishing broadening since it is the time Fourier transform of a time dependent term. The coefficient of delta function is the space Fourier transforms of the scatterer distribution, taken at infinite time and averaged over all the possible initial positions. It has the dimension of a structure factor and gives the fraction of elastic component in total scattering function. Therefore, this coefficient is called Elastic Incoherent Structure Factor (EISF), which provides information about the geometry of the molecular motion.

In case, the motion is non-localized in space (like translational motion of bulk liquid) the probability of finding the particle at particular position $\boldsymbol{r}$ at long time $t\rightarrow\infty$ is zero provided that same particles was at $\boldsymbol{r}$=0 at time t=0. Therefore, a characteristic feature of the scattered intensity from a liquid or any material with translational disorder is the absence of elastic peak. Conversely the existence of an elastic component in the scattered intensity clearly indicates the presence of localized motion provided that elastic scattering is not due to immobile host.

In practice, for any QENS experiment, because of the finite instrumental resolution, $R(\omega)$, the scattered intensity can be represented as

$$I = S_{inc}(\boldsymbol{Q},\omega)\otimes R(\omega) = I_{inc}(\boldsymbol{Q},\infty)R(\omega) + S'_{inc}(\boldsymbol{Q},\omega)\otimes R(\omega) \tag{7}$$

$R(\omega)$ is generally obtained by measuring spectra from the standard vanadium sample which is largely an incoherent scatterer. Eq. (7) indicates that the elastic peak in the spectra does not appear as an infinitely sharp line but as a peak shaped curve, often approximated by some function (e.g. Gaussian) with an energy width characteristic of the instrument. This width ($\Delta E \sim 1/\Delta t$) defines the magnitude of the time-scale over which the motions are observable. As can be seen in later section, width of the quasielastic component in Eq. (7) is inversely proportional to the characteristic time of the motion. This means that the very slow motion corresponding to large characteristic time leads to negligible quasielastic broadening over the instrument resolution function. Therefore, corresponding scattered intensity is almost elastic. On the other hand, very fast motions produce considerable large broadening in comparison to the resolution function and will contribute to a flat background in the quasielastic region (depending on the available energy transfer range of the instrument). Thus, the energy resolution functions and available energy transfer range of instrument defines both upper and lower limits on the time scale of motion that can be observed with the spectrometer. Therefore, it is very important to choose an appropriate spectrometer to observe the possible stochastic dynamics with a particular relaxation time. It is possible to separate the contributions from slow and fast motions by using spectrometers having different energy resolutions. The slow motion could be investigated with high resolution instrument where the faster motion would contribute as background. The data with poor resolution instrument will have contribution from both slow and fast motions, but in the analysis, one could use the information as obtained from the high-resolution instrument for the slower motion and obtain information pertaining to that of the faster one.

For a molecular system, several kinds of motions viz. translational, rotational and vibrational can simultaneously exist. In general, diffusional (translational or rotational) and vibrational motions are assumed to be dynamically independent of each other because they occur on clearly different time scales. Further, dynamical coupling between translational and rotational motion is neglected. In that case, one can write incoherent part of the intermediate scattering function as [2-3],

$$I_{inc}(\boldsymbol{Q},t) = I^{T}_{inc}(\boldsymbol{Q},t).I^{R}_{inc}(\boldsymbol{Q},t).I^{V}_{inc}(\boldsymbol{Q},t) \tag{8}$$

where the superscripts T, R and V refer to the translational, rotational and vibrational components respectively. The above equation can be written also in terms of $S_{inc}(\boldsymbol{Q},\omega)$ as,

$$S_{inc}(\boldsymbol{Q},\omega) = S^{T}_{inc}(\boldsymbol{Q},\omega)\otimes S^{R}_{inc}(\boldsymbol{Q},\omega)\otimes S^{V}_{inc}(\boldsymbol{Q},\omega) \tag{9}$$

where the symbol $\otimes$ stands for a convolution product. The scattering function of the vibrations contains an elastic term (associated with neutrons scattered without energy transfer) and inelastic terms (at the certain characteristic frequencies) and can be written as [2]

$$S^{V}_{inc}(\boldsymbol{Q},\omega) = \exp\{-2W(Q)\}\left[\delta(\omega) + S^{V'}_{inel}(\boldsymbol{Q},\omega)\right] \tag{10}$$

Here, *W(Q)* is the Debye-waller factor. $S_{inel}^{V'}(\mathbf{Q},\omega)$ is composed of a series of sharp peaks occurring at characteristic frequency ω_i of the system. From Eqs. (9) and (10), scattering law can be written as [2]

$$S_{inc}(\boldsymbol{Q},\omega) = \exp\{-2W(Q)\}\left[S_{inc}^{T}(\boldsymbol{Q},\omega) \otimes S_{inc}^{R}(\boldsymbol{Q},\omega) + S_{inc}^{I}(\boldsymbol{Q},\omega)\right] \quad (11)$$

The term $S_{inc}^{I}(\mathbf{Q},\omega)$ is an inelastic term that results from convolution of $S_{inc}^{V'}(\mathbf{Q},\omega)$ with $S_{inc}^{T}(\mathbf{Q},\omega) \otimes S_{inc}^{R}(\mathbf{Q},\omega)$. This term contributes very little in the quasielastic region (~± 2 meV) apart from possible increase in the background. Therefore, in the quasielastic regime, the Eq.(11) can be written as,

$$S_{inc}(Q,\omega) = \exp(-2W(Q))[S_{inc}^{T}(\boldsymbol{Q},\omega) \otimes S_{inc}^{R}(\boldsymbol{Q},\omega)] \quad (12)$$

Thus, in the quasielastic regime, the vibrational contribution will be only through the Debye-Waller factor, which is simply a scaling factor that does not modify the shape of the scattering function.

3. QENS Spectrometer at Dhruva

Neutron experiments, particularly those involving inelastic scattering, face a significant challenge related to the intensity of the neutron flux, especially in medium flux reactors like Dhruva [5], which serves as a national facility for conducting neutron beam research in India. The large size of the Dhruva reactor core results in a reduction of incident neutron flux on the monochromator itself, owing to various factors stemming from an exceptionally low solid angle subtended. Additionally, neutron beams extracted from the periphery of the reactor core, such as from tangential and radial. beam ports, suffer further losses due to the cosine-shaped distribution of neutron flux in a reactor. To address this issue and to enhance the neutron intensity for the QENS, several measures have been implemented

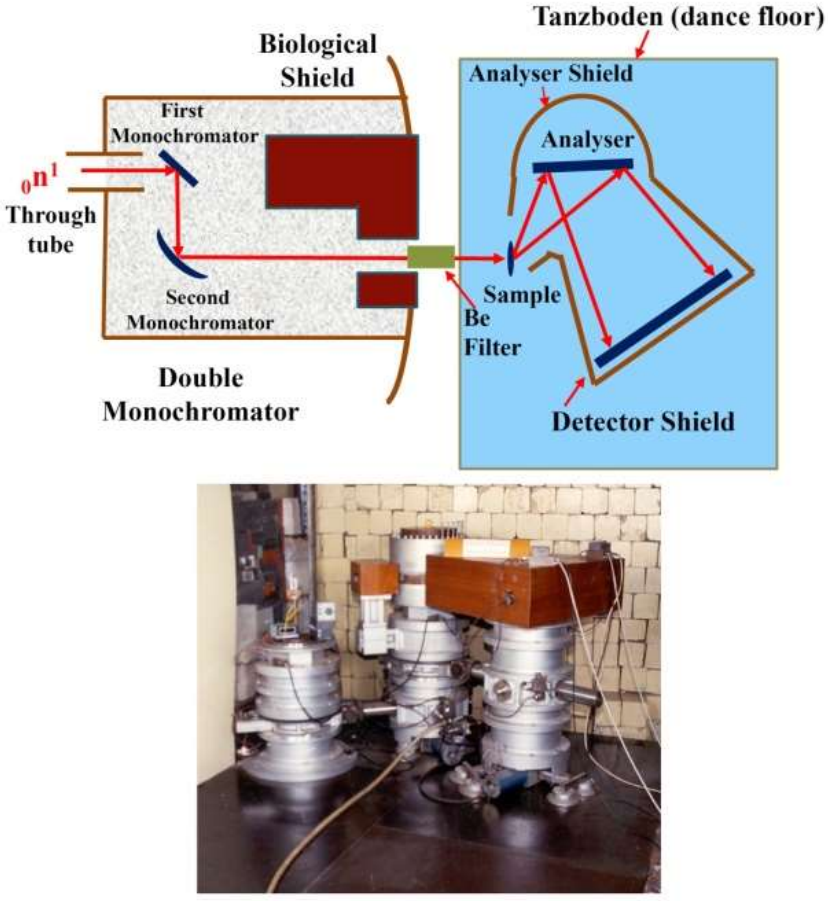

Fig. 2 Schematic and photograph of QENS spectrometer at Dhruva.

for the QENS spectrometer [6] at Dhruva, Trombay. For instance, the spectrometer is strategically positioned at the end of the through tube TT1004, where the emitted beam exhibits a significantly higher thermal neutron to fast neutron and gamma component compared to beams from tangential or radial holes. The next step in intensifying the neutron beam involves a closer proximity to the neutron source and employing a focusing monochromator. QENS spectrometer [6] incorporates a double monochromator arrangement, featuring pyrolytic graphite (002) crystals, positioned within a biological shield to enable a closer approach to the neutron source. The dual monochromator design ensures the availability of various incident wavelengths at a fixed sample position. The second monochromator is vertically bent to focus the neutron beam at the sample position. The scattered neutrons undergo energy selection through a large analyzer crystal and are then detected by a position-sensitive detector (PSD) using the Multi-Angle Reflecting X-tal (MARX) mode for energy analysis. Hence, QENS spectrometer at Dhruva is also referred as MARX spectrometer [6]. Since the analyzer crystal is large, each point along the length of the analyzer crystal will provide a different Bragg angle and reflect neutrons with different final energies. Thus, an energy scale is set up along the length of the detector and the spectrometer provides a broad energy spectrum for one instrumental configuration. Hence, the combination of a large analyzer crystal and a position-sensitive detector enables the spectrometer to provide a comprehensive energy spectrum for a single instrumental configuration, making it ideal for QENS experiments in a medium flux reactor. The out-of-pile section of the spectrometer is supported on an air cushion, facilitating adjustments to the scattering angle. Both the analyzer and the PSD rest on air pads located on a floor composed of machined and polished MS plates. A pressure of 6 kg/cm^2 is applied to energize the air pads, which are controlled by various pneumatic valves and cylinders. The schematic diagram along with the photograph of the spectrometer is shown in Fig. 2. MARX spectrometer was designed and fabricated indigenously at BARC. The spectrometer is being used regularly for studying the stochastic molecular motions in condensed matter systems. Key instrument parameters are detailed in Table-1. For 4 Å wavelength of the incident neutrons (E_i=5.1 meV), the energy resolution of the spectrometer is about 200 μeV and the wave vector transfer range available is 0.6-1.8 Å^{-1}. For 4 Å wavelengths of the incident neutrons, a beryllium filter is employed to eliminate neutrons with wavelengths smaller than 4 Å before reaching the sample.

Table-1 Instrument parameters [6]

Beam hole number	TT1004
Monochromators	2 PG (002) monochromators (100×80 mm^2) in tandem. 2nd one is vertically focused
$\lambda_{incident}$	1.3-4.7 Å
Scattering angle	$2\theta<80°$
Flux at sample	5×10^5 n/cm^2/s
Analyser	PG (002) (MARX mode)
Energy transfer range	2.3 meV (for E_i=5 meV)
Energy resolution ($\Delta E/E$)	~4 % (for E_i=5 meV; ΔE=200μeV)

4. Selected Examples studied at QENS Spectrometer, Dhruva at Trombay

4.1 Monolayer protected metal clusters [7-12]

Self-assembled monolayers (SAMs) are the molecular assemblies, which form spontaneously by immersion of an appropriate substrate into a solution of active surfactant. The classification of the structure and properties of SAMs is based on the dimensionality, i.e., two-dimensional (2D) SAMs and three-dimensional (3D) SAMs. The 2D SAMs are ordered molecular assemblies formed by the adsorption of an active surfactant on a planar solid substrate. The 3D SAMs are monolayers of surfactants formed on a nanosized metal core; the whole system together is called the monolayer protected metal clusters (MPCs). It is seen that the structure of the MPCs depend on the core material. For example, silver core MPCs form superlattices where gold core MPCs form isolated clusters. The monolayers have two distinct regions; 1) the thiol group which binds the monolayer to the surface of the cluster core, 2) the monolayer body (alkyl chains) which interacts with the adjacent chains through van der Waals interactions. Although the alkyl chain assembly is assumed to be all-*trans* in longer chain monolayers, the chains are found to be rotationally disordered. Temperature dependent phase behavior of MPC is intimately related to the evolution of dynamics of the alkyl chains with temperature because the rotator phase changes its nature at different temperatures. QENS experiments were carried out using MARX spectrometer at Dhruva, Trombay in order to understand how the dynamics of alkyl chain evolves with temperature for different MPCs, namely superlattices, isolated clusters and planer 2D thiolates [7-9]

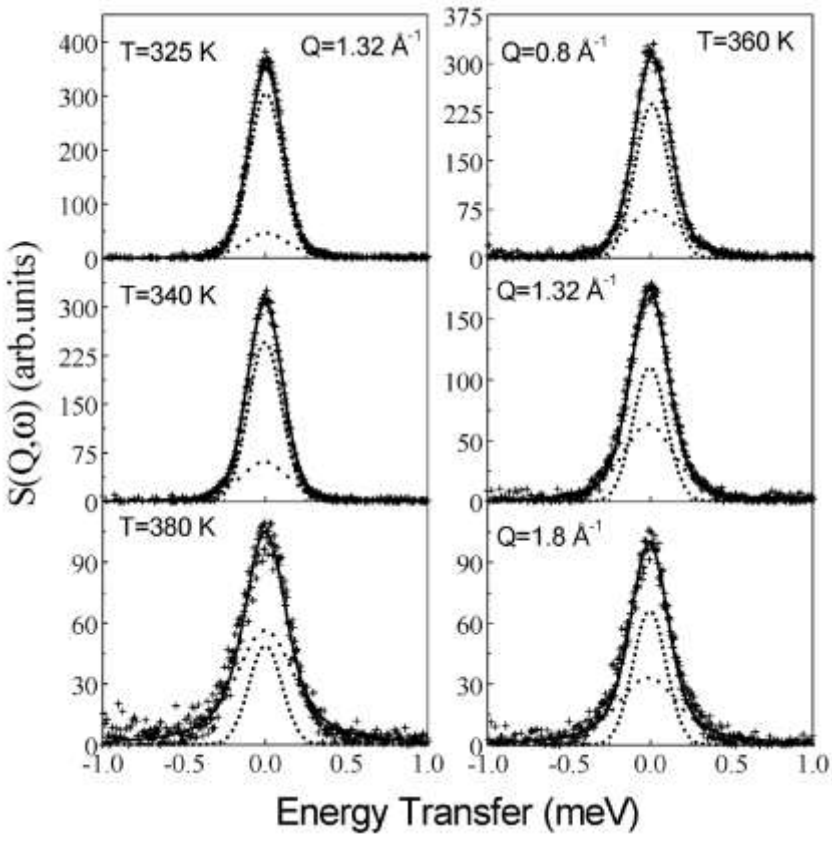

Fig. 3 Typical Fitted QENS spectra for AuHT, displaying an elastic (dotted) and quasielastic (dashed) components, observed at various temperatures at Q = 1.32 Å^{-1}, along with different Q values at T = 360 K.

4.1.1 Isolated Monolayer-Protected Gold Clusters: Gold clusters with different alkyl chain lengths studied through QENS techniques were AuC_6 (AuHT), AuC_8 (AuOT), AuC_{12} (AuDDT), and AuC_{18} (AuODT) (C_n corresponds to the chain length of the thiol used). Typical observed QENS spectra for AuHT is shown in Fig. 3 at different temperatures at Q=1.32 $Å^{-1}$ and at different Q values at 360 K. Below 325 K, no significant QE broadening was observed suggesting the absence of any stochastic motion within the energy resolution of the spectrometer. However, above 325 K, significant quasielastic broadening was observed. Eq. (7) was used to separate elastic and quasielastic components for AuHT and separated components are shown in Fig. 3. Significant fraction of elastic component was observed suggesting the presence of localised dynamics. EISF is obtained from fraction of elastic intensity and were analyzed assuming possible models [8]. The variations of EISF with Q at different temperatures in the case of AuHT are shown in Fig. 4 (a). It is clear that the EISF changes with temperature, which suggests that the geometry of rotation is different at different temperatures. Since EISF is the measure of the elastic component in the total spectrum, a large EISF means less quasielastic component, which may imply that the contribution to the dynamics is less and vice versa. Various rotational models were considered to explain the observed EISF. It was found that uniaxial rotational diffusional model works best. It was also found that at lower temperature not all the alkyl chains are mobile and as the temperatures increases, more and more alkyl chains participate in the dynamics. It was observed that at 325 K, only 25% alkyl chain participate in the dynamics while at 400 K all the alkyl chains are mobile enough to contribute to the QENS spectra. It is also found that as the chain length is increased, a larger number of alkyl chains are participating in the dynamics at lower temperature. For example, in case of AuDDT (AuC12), it is found that about 70% of the chains contribute to the dynamics at 325 K.

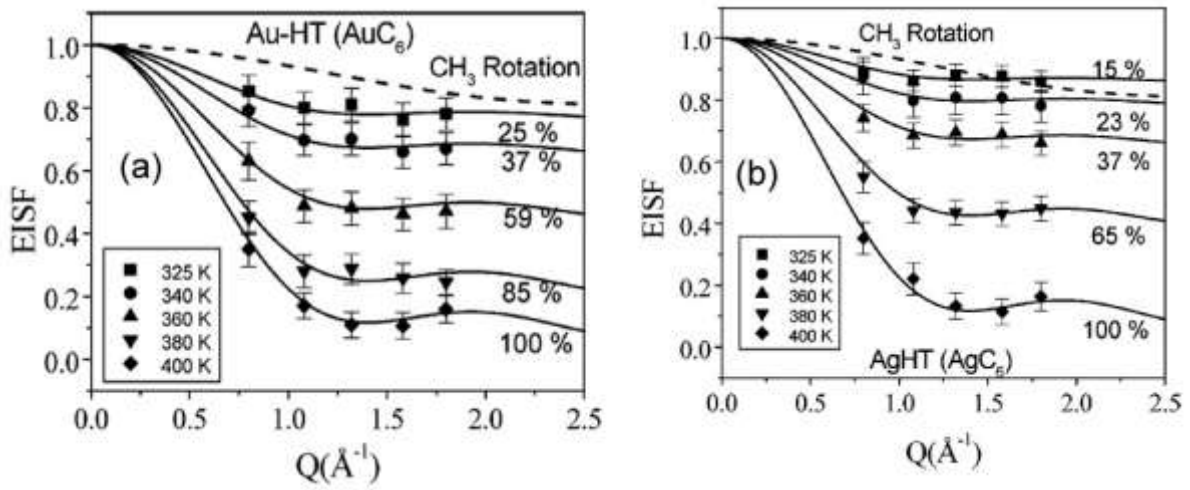

Fig. 4 Variation of EISF with Q at different temperatures for (a) Au-HT and (b) Ag-HT. The dashed line is the calculated EISF assuming rotation of the CH_3 group alone. Solid lines are the fits with fractional uniaxial rotational diffusion model. The proportion of the protons contributing to the dynamics is indicated at each temperature.

4.1.2 Superlattice Systems. MPCs with silver clusters form superlattice structures by virtue of the interdigitation of the neighboring chains. QENS experiments were carried out on various superlattice systems such as AgC_6 (AuHT), AgC_8 (AuOT), AgC_{12} (AgDDT), and AgC_{18} (AgODT) using MARX spectrometer at Dhruva, Trombay [7-9]. The variation of EISF for AgC_6 (AgHT) at different temperatures is shown in Fig. 4 (b). Fractional uniaxial rotational diffusion is used to describe EISF and is also shown in Fig. 4 (b) [8]. The proportion of the mobile chain as obtained from the fit of the measured EISF is indicated in the figure. It is found that at 325 K, only 15% of the chains are dynamic. The dynamical component increases with temperature, and finally all the chains are dynamic at 400 K, which is, anyway, the superlattice melting point. In the case of the next longer chain system, AgOT, QE broadening was observed even at 300 K. Analysis showed that 50% of the chains

contribute to the dynamics and do not take part in interdigitation. This is inferred from the fact that the ratio of the interdigitated to non-interdigitated chains is also 50% as obtained from the geometry of the structure in a simple cubic lattice. With increasing temperature, more and more chains started contributing to the dynamics, and eventually at 380 K all the chains were dynamic. A few interesting things were noticed in the case of the superlattice systems, AgDDT and AgODT. While quasielastic broadening is observed at room temperature in the case of AgDDT, no quasielastic broadening is seen in AgODT at room temperature. Partial melting of the chains is observed at different temperatures lower than 380 K in both the systems. Most interestingly, in both the systems, time-dependent partial melting is observed at 380 K. It is seen that, even at a constant temperature, the proportion of chains contributing to the dynamics increases slowly with time. Thus, there appears to be a nearly thermoneutral event involving the alkyl chains at this temperature. This could also be (additionally) associated with cluster surface annealing as morphology changes are seen in the clusters upon heating.

4.2 Liquid Crystals [12-16]

Liquid Crystals are a state of matter that exhibits properties between those of conventional liquids and solid crystals. Their unique molecular arrangement imparts the ability to flow like a liquid while maintaining some degree of order seen in crystalline structures. Liquid crystals have garnered significant attention due to their responsiveness to external stimuli, enabling applications in display technologies, sensors, and optical devices, making them essential in modern electronics and materials science. Liquid crystalline systems usually present a number of different mesophases, which differ by the degree of randomness of the molecular motion. It is of interest to understand the details of the microscopic motion in the different mesophases to understand the various properties of liquid crystal. QENS technique is very suitable to study these microscopic motions for its matching time scale and large scattering cross-section of the protons. The reorientational motions of different nO.m (alkyloxy benzylidine alkylanilenes) type liquid crystal systems, viz. 4O.4, 4O.8, 5O.6 and 6O4 in their different mesomorphic phases were studied using MARX spectrometer at Dhruva, Trombay [12-16]. The 6O.4 molecular configuration is schematized in its trans conformation in Fig. 5(a). Three different possible axes of rotations are shown. The transition scheme in 6O.4 as reported by Leadbetter et al. [17] is, $K \xrightarrow{30C} S_H \xrightarrow{57C} S_B \xrightarrow{59C} S_A \xrightarrow{70C} N \xrightarrow{78C} I$. Here, *K*, *S*, *N* and *I* represent the crystalline, smectic, nematic and isotropic phases respectively. Quasielastic experiments for 6O.4 liquid crystal were performed in crystalline (room temperature) and in smectic H (45 °C) [13]. QENS measurements were also performed at room temperature after cooling the sample from high temperature. This is to ascertain whether the dynamical transition is reversible. Quasielastic broadening was observed in both the phases. QENS data were separated into elastic and quasielastic part and EISF were extracted for both the phases. The EISF values as obtained from the fit of the experimental data correspond to RT, 45°C and cooled back to RT are shown in Fig. 5(b). To explain the observed EISF, various dynamical situations with respect to the core and chains belonging to 6O.4 (Fig. 5(a)) were considered, like, core of the molecule rotating side chains static and vice versa, side chain can rotate about its own axis (line AB or EF) or about the molecular axis (line CD), core and chain move either independently or in unison, etc. In the crystalline phase, a model where the hydrogen atoms only belonging to the core undergoing rotation about the core axis (line CD in Fig. 5(a)) describes the data consistently. Data corresponding to the S_H phase show much higher disorder compared to the crystalline phase. As noted earlier, the side chains also can rotate about their respective axes in addition or independent of the core motion. In the case of smectic H phase of 6O.4, the model in which the whole molecule (core + side chain) rotate about the molecular axis and the side chains rotate about their respective axes, describes the behavior of EISF the best. It is also found that when the sample was cooled from 45°C to room temperature (below the K–S_H transition temperature) the data still correspond to that of the S_H phase indicating that this phase exists as a metastable state at room temperature. DSC measurements corroborate that a physically stable liquid crystalline phase (S_H) is formed at 33.7 °C which does not go to the crystalline phase even after cooling the sample. The initial phase at 25°C is

found to be crystalline consistent with monoclinic structure and transforms to S_H phase in which the packing is hexagonal as indicated in the XRD study. This demonstrates that what was observed in the microscopic measurement like QENS was later confirmed by the macroscopic technique like DSC. XRD studies reconfirmed both the results.

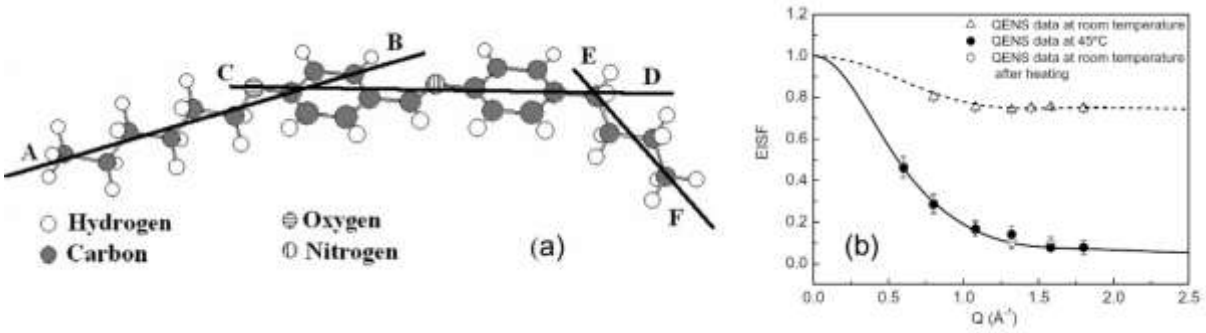

Fig. 5 (a) Schematic of the liquid crystal 6O.4 molecule. Three different possible axes of rotations are shown. AB axis is the hexyloxy chain axis, CD axis is the molecular or core axis and EF axis is the butyl chain axis. (b) Variation of EISF with *Q*. The lines correspond to model functions and the symbols are the experimental data at different temperatures.

4.3 Confined Fluids [18-65]

Fluids constrained within a spatial medium are termed as confined fluids, exhibiting distinct behavior from their bulk counterparts. Factors such as freezing behavior, sorption, wetting, and structural dynamics, including diffusion and relaxation, undergo modification under confinement [66]. The interplay between spatial restriction and guest-host interactions predominantly governs the behavior of fluids in restricted geometries. This alteration in the dynamic behavior of confined fluids, compared to their bulk counterparts, holds significant interest in scientific research, addressing both fundamental aspects and practical applications in industries such as petroleum, catalysis, and water purification. Aluminosilicates are prevalent components in everyday rocks, and through weathering, various types of clays can be generated [18]. These materials are recognized for their layered and porous structures, making them ideal for investigating sorbate diffusion in confined systems. Among aluminosilicate materials, zeolites and clays stand out as two distinct classes, each offering well-ordered porous or layered structures, respectively. Zeolitic materials are notable for their high catalytic activity and molecular sieving properties, while clay materials find applications in catalysis, desalination, enhanced oil recovery, and creating barriers in radioactive waste disposal. QENS spectrometer at Dhruva has been widely used to understand diffusion mechanism of many fluids such as hydrocarbons, water in various nanoscopic regimes including zeolites, clays, water filtration membranes. We have written comprehensive review articles on confined fluids mainly based on the studies carried out at QENS spectrometer at Dhruva [18-21]. Here, we shall discuss few selected examples on the confined fluids. We divided this section into two subsections. First, we shall discuss about confined water and in second, we shall discuss about confined hydrocarbons in zeolites.

4.3.1 Dynamics of Water in various Nanoscopic Regimes [22-39]

Natural occurrences, such as water confined in rock crevices or within cells, exemplify this class of systems, where confined water is vital for cellular function. Investigating the impact of confinement on the properties of water becomes particularly intriguing in such contexts. Our investigation delves into the dynamics of confined water within a range of important materials such as water filtration membranes [22-24], MCM-41 [25], clays [26-33], molecular magnets [34-36] porous alumina [37-38], coal [39], Portland cement [40]. The study reveals distinct dynamical properties of water when confined at the nanoscopic scale, a phenomenon attributed to factors like geometric restriction, host topology, and interactions between water and the hosting material. Few selected example of water in restricted geometries is discussed below.

4.3.1.1 Water Filtration Membranes [22-24]:

Nanoporous polyamide membranes find extensive applications in the removal of organic substances from natural and waste water, desalination of sea and brackish waters, and treatment of industrial effluents, among other uses [41]. These membranes are also employed in the filtration of drinking water. The filtration process induces a complex transformation in the self-diffusion mechanism of water molecules as they traverse the membrane. The effectiveness of these membranes in the filtration process relies on their water uptake capacity, making it essential to investigate the dynamic behavior of water within these membranes. In our study, we concentrated on two specific polyamide membranes: (i) a reverse osmosis (RO) membrane based on trimesoyl chloride - m-phenylene diamine, and (ii) a nanofiltration (NF) membrane based on trimesoyl chloride - piperazine. The pore size of both membranes is approximately 5 Å, determined using positron annihilation lifetime spectroscopy. To investigate the dynamics of water within these polyamide membranes, QENS experiments were conducted on both dehydrated (bare) RO and NF polyamide membranes using MARX spectrometer, Dhruva at Trombay [22,23]. The membranes were hydrated by saturating them with distilled water, and QENS measurements were performed on both water-sorbed RO and NF polyamide membranes. The QENS spectra for dehydrated polyamide membranes did not show quasielastic broadening, whereas the water-sorbed membranes exhibited significant quasielastic broadening beyond the instrument resolution. The analysis involved separating the elastic and quasielastic contributions. Data from dehydrated polyamide membrane sample were used to estimate the contributions of dehydrated membrane to the total spectra. Elastic component corresponding to water diffusion is found to be insignificant and a single Lorentzian function adequately fit the data in both cases, indicating that the observed dynamics at MARX spectrometer mainly result from the translational motion of water.

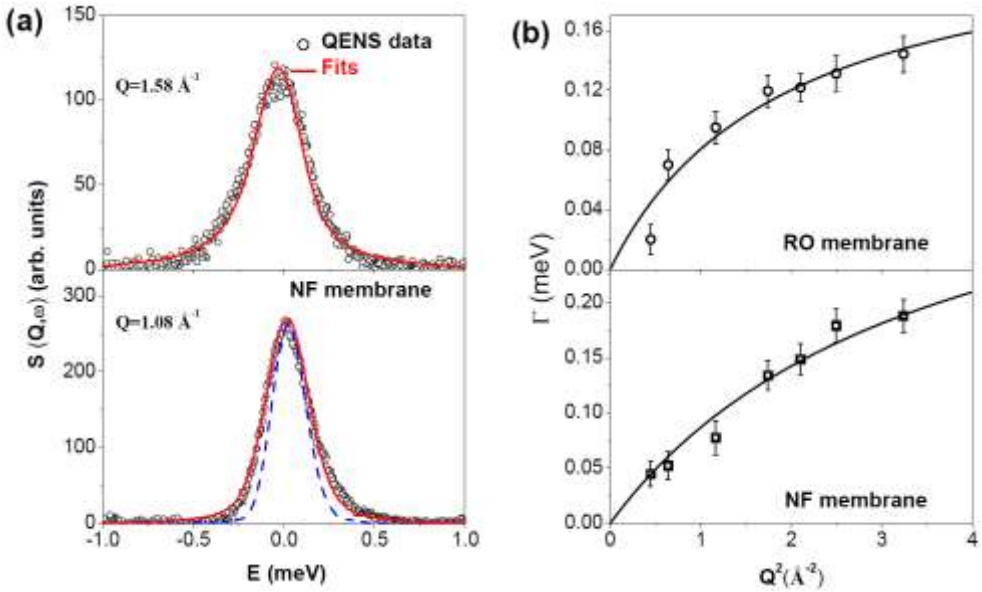

Fig. 6 (a) Typical fitted QENS spectra from the water-sorbed NF polyamide membrane at some typical *Q*-values. Instrument resolution is shown by dashed line in the lower panel. (b) Variation of HWHM (Γ), with Q^2 for water sorbed in RO and NF polyamide membranes. The symbols represent experimental Γ values while the solid line is the fit with Singwi-Sjölander model.

Typical fits of QENS data for NF membrane at two different *Q* values are shown in Fig. 6 (a) [22-23]. The Half Width at Half Maximum (HWHM's) of the Lorentzian (Γ) obtained from the fits for both RO and NF membranes are shown in Fig. 6(b) [22,23]. At higher *Q* values, a deviation from linear behavior ($\Gamma = DQ^2$, following Fick's law) was observed. To describe the water dynamics in polyamide membranes, a jump diffusion model was employed; in which particle remain at a site for a residence time before instantaneously jumping to another site. The random jump length distribution,

modeled by the Singwi-Sjölander (SS) model of jump diffusion, effectively described the water diffusion in both RO and NF membrane systems. Translational diffusion coefficient (D) and residence time (τ) were obtained from the fits. For the RO membrane, D and τ were found to be $(1.9\pm0.4)\times10^{-5}$ cm²/s and (2.8±0.6) ps, respectively [22]. In the case of water diffusion in the NF membrane, D and τ were determined to be $(1.4\pm0.3)\times 10^{-5}$ cm²/s and (1.1±0.3) ps, respectively [23]. We have further investigated these systems using different energy resolution QENS spectrometer which help us to disentangle translational as well as the rotational motion [24].

4.3.1.2 Clays [26-33]:

Understanding the dynamics of water confined within clay minerals is crucial for gaining insights into the transport properties of water and dissolved components within constrained environments. This knowledge holds significant implications for the management and disposal of radioactive waste. We have investigated dynamic behavior of water in various clay minerals, including saponite [26-30], bentonite [31], and hydrotalcite [32,33] using QENS techniques. Saponite and bentonite clays are members of the smectite mineral family characterized by a 2:1 layer structure. In this structure, an octahedral layer of Al and Mg, sandwiched between two tetrahedral alumino-silicate layers. These layers exhibit a net negative charge framework, resulting from the substitution of Si(IV) in the tetrahedral layers with Al(III) or Fe(III) ions. The anionic framework charge on the sheets is offset by the presence of appropriately charged cations, which exist in their hydrated forms within the interlamellar space.

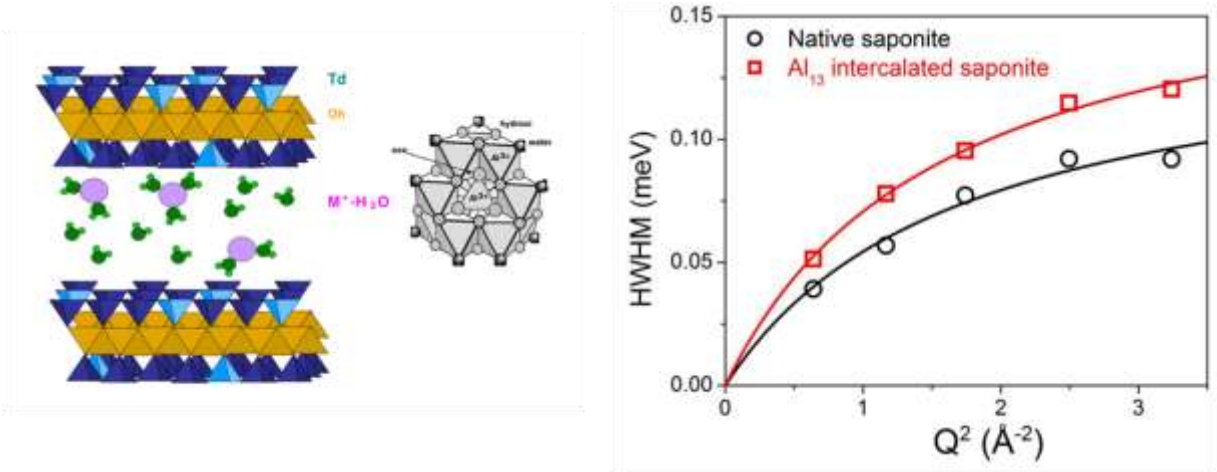

Fig. 7 (Left) Schematic depiction of natural smectitic clay, showcasing its essential components: the tetrahedral sheet (Td), octahedral sheet (Oh), and hydrated exchangeable cations (M^+-H_2O). Additionally, the figure illustrates the tridecameric $[Al_{13}O_4(OH)_{24}(H_2O)_{12}]^{7+}$ polycation. (Right) The variation of HWHM for the translational components with Q^2 is depicted, with solid lines representing the fitting results using the jump diffusion process.

Saponite clay in a native state and with tridecameric 'Al_{13}' intercalated polycation were synthesized. X-ray diffraction studies revealed an increased interlayer spacing in Al_{13} intercalated saponite (18.1 Å) compared to its native counterpart (14.4 Å) [26]. Room temperature QENS experiments were conducted on both native saponite clays and its tridecameric 'Al_{13}' intercalated polycation using MARX spectrometer, Dhruva at Trombay [26]. QENS measurements were also carried out on dehydrated native saponite and Al_{13} intercalated saponite (after heating 150°C) to estimate the contribution of host itself. No quasielastic broadening was observed for dehydrated samples whereas hydrated samples show significant quasielastic broadening suggesting observed broadening correspond to dynamics of water only. The variation of HWHM of the translational component with Q^2 for both native saponite and intercalated saponite is shown in Fig. 7. A model incorporating random jump diffusion accurately describes the translational motion of water molecules in both clays, with the diffusivity found to be lower than that of bulk water. A comparative analysis

of water molecule diffusivity in the two clays indicates a larger value in Al_{13} intercalated saponite (1.8×10^{-5} cm²/sec) compared to native saponite (1.3×10^{-5} cm²/sec) [26]. This difference is attributed to the expanded interlayer spacing in the intercalated compound, as demonstrated by experimental findings [26].

QENS measurements were also carried out on synthetic saponite clays which have distinct advantages over natural clays [27-29]. Synthetic saponites, designated as SapNi and SapMg, were prepared with Ni^{2+} and Mg^{2+} respectively positioned at octahedral sites. These clays were microwave-treated, resulting in interlayer spacing of 12 Å for SapNi and 16 Å for SapMg [27]. QENS experiments were performed on both SapNi and SapMg using the MARX spectrometer at Dhruva to explore the dynamics of water within these structures [27]. The investigations revealed that the dynamics of water in both saponite samples are hindered compared to bulk water. Upon comparison, the diffusivity of water was found to be greater in SapMg (1.8×10^{-5} cm²/sec) in comparison to SapNi (0.9×10^{-5} cm²/sec) [27]. It may be noted that SAPMg (16 Å) has a larger interlayer spacing than SapNi (12 Å). These findings suggest a strong dependence of water dynamics on interlayer spacing in clay, indicating that as the spacing between layers increases, the diffusivity of water also increases.

We have also investigated the role of other parameter such as concentration of charge balancing cation on the dynamics of water [30]. QENS experiments were conducted on two synthetic saponite clays, namely $[Si_{6.97}Al_{1.03}][Ni_{6.00}]O_{20}(OH)_4[Na_{1.03}].28H_2O$ (SAP-1) and $[Si_{7.13}Fe_{0.86}][Ni_{6.00}]O_{20}(OH)_4[Na_{0.86}].14H_2O$ (SAP-2), each containing varying concentrations of charge-balancing cations (Na^+) within their interlayer spaces [30]. Despite having similar interlayer spacings, as confirmed by X-ray diffraction studies, SAP-1 exhibited a lower diffusivity of water (0.65×10^{-5} cm²/sec at 293 K) compared to SAP-2 (1.26×10^{-5} cm²/sec at 293 K) [30]. The reduction in water diffusivity in SAP-1, as opposed to SAP-2, can be elucidated based on the net charge on the tetrahedral layers and the corresponding number of charge-balancing cations within the interlayer spacing. Since these cations exist in a hydrated form, the fraction of water molecules in the hydration shells around the cations increases. Water molecules within these hydration shells exhibit limited mobility, resulting in a decrease in the average diffusivity of mobile water molecules in clays with a higher concentration of charge-balancing cations.

Our QENS studies at MARX spectrometer on hydrotalcite with varying water contents shown as the amount of water increases, translational diffusivity of water increases [32,33] Our studies on clays revealed that the nature of water molecule diffusion in clays influenced by various factors such as interlayer spacing, hydration level, and the presence of charge balancing cations.

4.3.2 Confined Fluids in Zeolites [18, 21, 42-66]

Zeolites, classified as aluminosilicates, belong to the family of microporous solids referred to as "molecular sieves," primarily composed of Si, Al, and O. The remarkable catalytic and molecular sieving properties of zeolitic materials are attributed to their high surface area, solid acid functionality, and shape selectivity, all stemming from their intricate porous architecture. The catalytic and molecular sieving properties of zeolites hinge primarily on the diffusivity of adsorbed molecules. Beyond their practical applications, the ordered porous structure of zeolites positions them as ideal subjects for studying the impact of confinement. Our investigation explores into the diffusion of diverse guest species confined within distinct host matrices, employing QENS experiments and molecular dynamics (MD) simulations. All QENS experiments on confined fluids in zeolites were conducted using our in-house developed MARX spectrometer [18, 21, 42-66] at Trombay. In our investigation, we selected several host matrices, including Na-Y, ZSM-5, and MCM-41 [18, 21, 42-66]. Na-Y zeolite features an intricate network of nearly spherical supercages (diameter ~11.8 Å), interconnected in a tetrahedral manner by windows (diameter ~7.8 Å) [18]. The ZSM-5 framework comprises straight channels (~5.7 Å) interconnected by sinusoidal channels (~5.4 Å), while MCM-41 molecular sieve possesses non-connecting channels with a size of 34 Å [18]. For example, schematic of the spherical cage in Na-Y zeolite and the channel structures of ZSM-5 zeolite are shown in Fig. 8 (a). These diverse systems offer an opportunity to investigate the transport of guest molecules in connected small cylindrical micropores (ZSM-5 zeolite), large spherical micropores (Na-Y zeolite), and non-

connected cylindrical mesopores (MCM-41). To explore the impact of the size and shape of guest molecules, we maintained same host matrix (Na-Y zeolite) and introduced different guest species (propane, acetylene, butadiene) [18,47-56]. Similarly, to investigate the influence of the host matrix, we conducted experiments with the same guest species (propylene) in different host matrices (Na-Y zeolite, ZSM-5 zeolite) [21,42]. MD simulation studies conducted by us [18,21,42,45,46] indicate that the rotational motion of propylene is nearly an order of magnitude faster than its translational motion. Consequently, we employed both QENS spectrometer (ΔE ~ 200 μeV) and a Triple Axis Spectrometer (TAS) (ΔE ~ 3 meV) at Trombay to gain insights into the translational and rotational motion of propylene [21,42]. The slower translational motion is distinctly observed in the narrower window of the QENS spectrometer, while both contribute to the broader window of the TAS spectrometer. Variations of HWHM corresponding to translational motion of propylene in Na-Y and ZSM-5 are shown in Fig. 8 (b). For direct comparison, HWHM corresponding to translational motion of acetylene in Na-Y is also shown in Fig. 8 (b). It is found that both acetylene and propylene in Na-Y follow jump diffusion but acetylene show relatively faster diffusivity compared to propylene which could be due to smaller size of acetylene. While comparing propylene in both zeolites, although the translational motion of propylene in both zeolites follows jump diffusion model, the diffusivity in ZSM-5 is three times lower than that in Na-Y zeolite. The reduced diffusivity may be attributed to greater geometric constraints in the case of ZSM-5 zeolite. The variation of the EISF (Fig. 8c) suggests that the rotational motion of propylene is isotropic in both zeolites. The EISF for propylene in Na-Y, obtained from both experiment and MD simulation, is illustrated in Fig.8 (c) [42,45,46]. However, in the case of ZSM-5 zeolite, intermediate scattering functions calculated from MD simulation indicate a complex and anisotropic rotational motion of propylene, especially at short times [46]. It is also observed that while diffusing in ZSM-5, propylene molecules exhibit a preference for an orientation in which the long molecular axis aligns along the channel. Furthermore, both translational and rotational motions of acetylene in Na-Y zeolite have been studied and found to be faster than propylene in Na-Y zeolite [18,42,45,46,52]. While the rotational diffusion of acetylene in Na-Y is isotropic, the microscopic features of rotational diffusion differ significantly [47]. For example, in the case of acetylene, the angular jump between two successive steps occurs through large rotations [47].

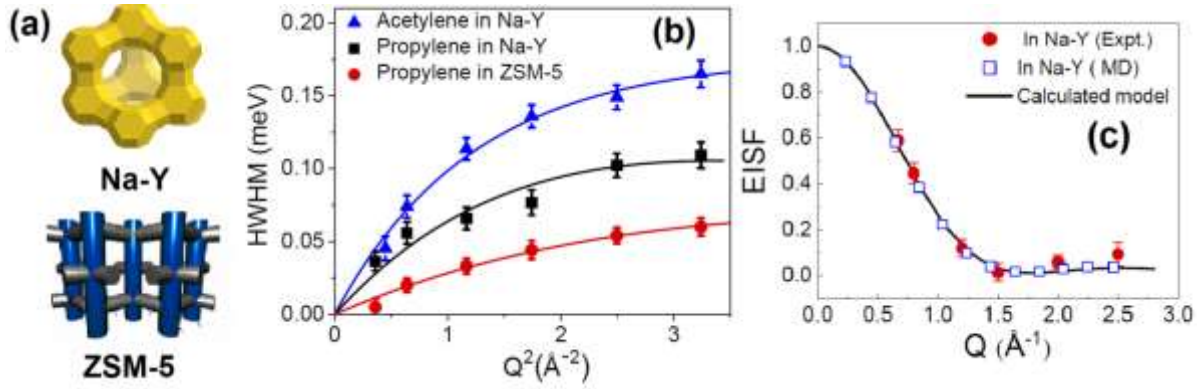

Fig. 8 (a) Schematic of the spherical cage in Na-Y zeolite and the channel structures of ZSM-5 zeolite.(b) Variation of quasielastic width corresponding to translational motion for acetylene in Na-Y zeolite and propylene in Na-Y and ZSM-5 zeolite at 300 K. The solid lines represent fits using the jump diffusion model (c) EISF for propylene in Na-Y zeolites obtained from both QENS experiments and MD simulations. The Solid line corresponds to the isotropic rotational diffusion model.

4.4 Complex Fluids [67-75]:

4.4.1 Deep Eutectic Solvents (DESs)[67-72]

The fundamental principle of contemporary sustainable development in science and industry revolves around the necessity for green solvent media. Among the recent addition in this area are deep eutectic solvents (DESs), which consist of mixtures of hydrogen bond donors (HBDs) and salts at a eutectic composition [67]. DESs predominantly exist in a liquid state at ambient conditions due to a significant decrease in the freezing points of their parent compounds. The preparation procedures for DESs are

comparatively cost-effective and do not generate non-biodegradable waste. These solvents exhibit higher thermal stability, minimal volatility, low vapor pressures, and a notable capacity for dissolving various metals. DESs have demonstrated significant potential as liquid electrolytes in diverse applications, such as lithium-ion batteries, supercapacitors, and the electrodeposition of metals. The macroscopic transport properties of DES play a crucial role in these applications. We have written a perspective article on the reconciliation of macroscopic and microscopic transports on DES [67]. Our objective was to explore the microscopic dynamics of these systems through QENS and MD simulations, aiming to gain insights into the underlying mechanisms responsible for these bulk properties. QENS experiments were carried out on various DESs synthesized from acetamide and lithium based salts (e.g. $LiNO_3$, $LiClO_4$, etc.) using MARX spectrometer, Dhruva at Trombay to understand the diffusion mechanism of acetamide [68-70]. Our results indicated that extensive hydrogen bonding in the DES play an important role in the microscopic diffusion of DES and effectively modulate its bulk properties. This hydrogen bonding network can be modulated by addition of strong hydrogen bonded liquid (e.g. water). Water plays a multifaceted role in DES, contributing not only to the rearrangement of local molecular ordering but also influencing the dynamics and hydrogen-bonding interactions within the DES. We have investigated influence of water on the diffusion mechanism of acetamide in aqueous mixtures of DES synthesized with acetamide and lithium perchlorate [70-71]. The QENS spectra for two systems, namely DES (acetamide + lithium perchlorate) and DES + 20 wt% D_2O, observed at the MARX spectrometer, Dhruva, Trombay are depicted in the Fig 9(a) [70]. The QENS spectrometer facilitates the observation of dynamics within the timescale of a few picoseconds (1 to 15 ps). Our observations revealed contributions from the rotational diffusion of acetamide and localized fluctuation of acetamide center of mass within transient cages. To provide more microscopic insights, MD simulations were carried out, revealing an additional jump diffusion of acetamide across the cages [70-71]. Consequently, acetamide dynamics involve both localized diffusion within transient cages and a jump diffusion process across cages. Our results indicate a substantial enhancement in acetamide jump diffusion by approximately a factor of 10 with an increase in water content to 20 wt%. Meanwhile, the geometry

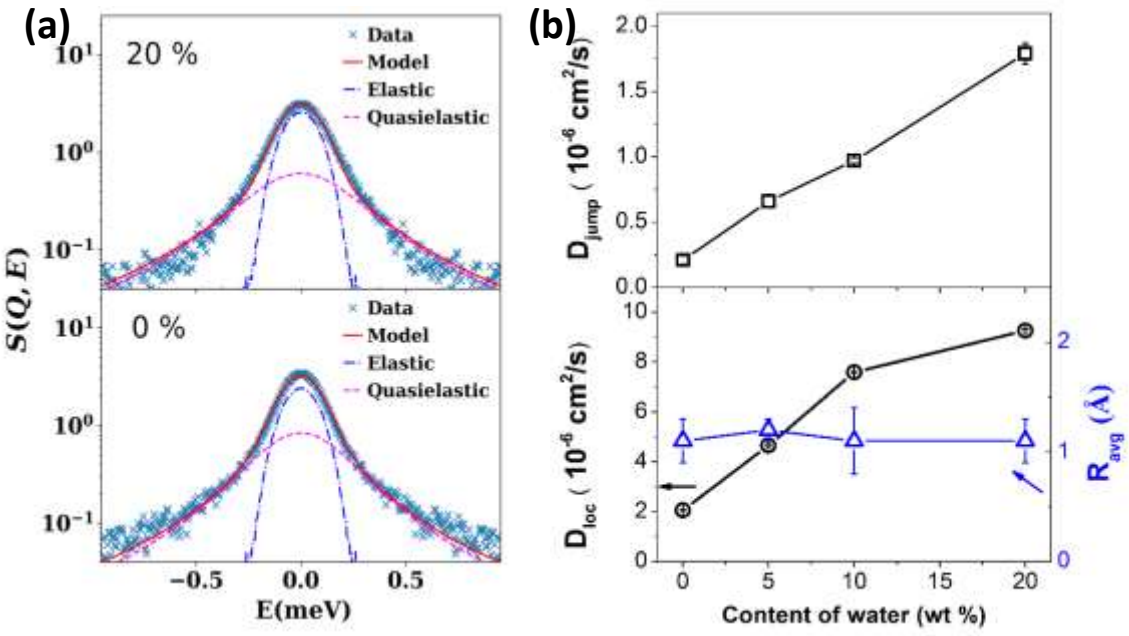

Fig. 9 (a) Fitted QENS spectra for pure DES and DES with 20% D_2O at a *Q*-value of 1.4 $Å^{-1}$. Individual components representing elastic and quasielastic contributions are also shown. (b) Variation of diffusion coefficient associated with jump diffusion (upper panel) and localized diffusion (bottom panel) with water content in DES. Additionally, the figure illustrates the variation in average radii of the confining sphere with water content.

of the localized dynamics remains unchanged with the addition of water, but the localized diffusion becomes significantly faster and more heterogeneous with increasing water concentration. The variation of the diffusion coefficient associated with acetamide jump diffusion and localized diffusion with water content is illustrated in the Fig 9(b) [70]. Additionally, we demonstrated the variation in the average confinement radius of acetamide with water content. Water concentration in the DES was found to control the solvation structure of lithium ions, with ions becoming significantly hydrated at 20 wt% water. The formation of inter-water and water-acetamide hydrogen bonds was observed. While the increase in water concentration increased the number of H-bonds, their lifetimes decreased substantially. Similarly, lifetimes of acetamide-lithium complexes diminished with increasing water concentration. A power-law scaling relationship between lifetimes and diffusion constants was established, elucidating the extent of coupling between diffusive processes and hydrogen bonding, as well as microscopic complexation. This study underscores the utility of water as a probe for investigating the role of structural relaxation and complex lifetimes in diffusive processes across different time and length scales.

4.4.2 Colloid and Slurry [73-75]: Utilizing aqueous colloidal shaping techniques like slip casting, gel casting, freeze casting, and direct coagulation casting is advantageous for fabricating ceramic components with intricate geometries. In the context of alumina slurry containing methyl cellulose, the gelation shaping process during temperature variation was investigated using QENS experiments at Trombay [73]. Rheological assessments of the alumina slurry revealed a sharp viscosity increase between 50°C and 55°C, while QENS studies indicated a decrease in water diffusivity at and above 55°C. The observed phenomena were attributed to irreversible gel formation involving cross-linked polymer-solvent interactions, correlating with the casting of consolidated green alumina parts.

Magnesium aluminate ($MgAl_2O_4$) spinel is a crucial material for ceramic casting, and its aqueous colloidal forming presents significant potential for diverse applications. However, challenges arise from the inherent nature of the powder, which tends to undergo hydrolysis. To address this, spinel

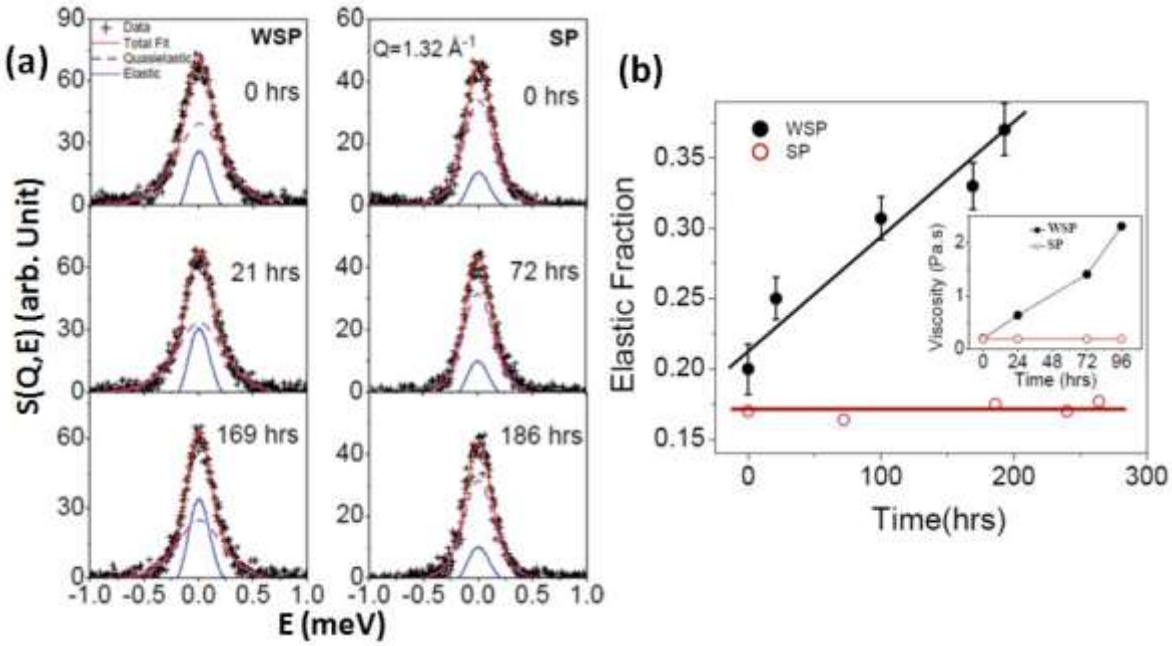

Fig. 10 (a) Typical fitted QENS spectra for slurries based on magnesium aluminate ($MgAl_2O_4$) spinel without surface passivation (WSP) and with surface passivation (SP) at Q=1.32 $Å^{-1}$, recorded at different time intervals. Notably, the elastic component fraction (depicted by the blue solid line) increases over time in the WSP slurry, while the SP slurry shows minimal change in the elastic component. (b) A plot of elastic fraction in QENS spectra and viscosity with time of SP and WSP spinel slurries.

powders underwent thermally assisted surface passivation, and the efficacy of preventing hydrolysis was evaluated using QENS and rheological measurements [74]. QENS measurements were conducted on both surface passivated (SP) and without surface passivated (WSP) magnesium aluminate spinel slurries using MARX spectrometer, Trombay [74]. QENS spectra were recorded from the zero hour (when the slurry was prepared) and continued up to 270 hours. Typical measured QENS spectra for both the slurries recorded at different times are shown in Fig. 10 (a) at Q=1.32 Å^{-1}. QENS data were separated into elastic and quasielastic components which are also depicted in the Figure. Over time, the WSP slurry exhibited an increasing fraction of elastic intensity, indicating the binding of more water molecules due to the formation of a network of pores. In contrast, the SP slurry showed no significant change in elastic intensity over the same period. This enhanced stability in the slurry with surface passivation is consistently observed in both time-dependent elastic intensity from QENS spectra and viscosity measurements, as depicted in Fig. 10(b). The collective findings from microscopic and macroscopic measurements underscore the effectiveness of surface passivation in inhibiting hydrolysis in spinel slurry [74].

4.5 Self Assembled Aggregates [76-106]

Molecular self-assembly refers to a process wherein a disordered system of preexisting molecules transforms into an organized structure through specific, local interactions among the molecules themselves. Self-assembled systems involving amphiphilic molecules, such as micelles, microemulsions, and vesicles, exhibit distinctive shapes that can be precisely characterized using the surfactant packing parameter, denoted as C_{pp} ($C_{\mathrm{pp}} = v/a_0 l_{\mathrm{c}}$). This parameter involves key factors: v representing the hydrocarbon chain volume, a_0 signifying the effective headgroup area, and l_{c} denoting the chain length. These self-assembled aggregates showcase various functional properties, including wetting, emulsification, and the release of solubilized drugs. These properties are intricately linked to the dynamic behavior of surfactants at the molecular level, sparking significant interest in the dynamics of such systems. Our research has focused on studying the dynamics of different types of self-assembled surfactant-based aggregates, such as micelles [76-83] and liposomes [84-106], utilizing the QENS spectrometer at Dhruva. Deuterated water (D_2O) has been used in preparing of these aggregates to minimize the scattering contribution from the solvent. The contribution originating from the surfactant aggregates was determined by subtracting the data obtained from the solvent (D_2O), measured under identical conditions. In the following section, we will provide a brief overview of the results obtained for micelles and liposomes.

4.5.1 Micelles [76-83]

Exploring the internal dynamics of micellar assemblies is crucial for comprehending diverse properties, such as the mechanism behind releasing solubilized drugs and micellar breaking time. We employed QENS technique to investigate into the dynamics of various ionic micellar solutions, including sodium dodecyl sulfate (SDS). QENS experiments were carried out using MARX spectrometer, Trombay on various concentrations of SDS micelles [76]. To minimize the solvent contribution in the observed QENS signal, these micelles were prepared in D_2O. Moreover, to estimate the solvent contribution, QENS measurements were also carried out on pure D_2O. Contribution for SDS micelles is obtained by removing the contribution of solvent. Significant quasielastic broadening is observed suggesting presence of stochastic molecular motion of SDS surfactant in the micelles [76]. Detailed data analysis suggested that observed dynamics correspond to segmental motion of the surfactant within the micelles. Typical fitted QENS spectra for SDS micelles is shown in Fig. 11.

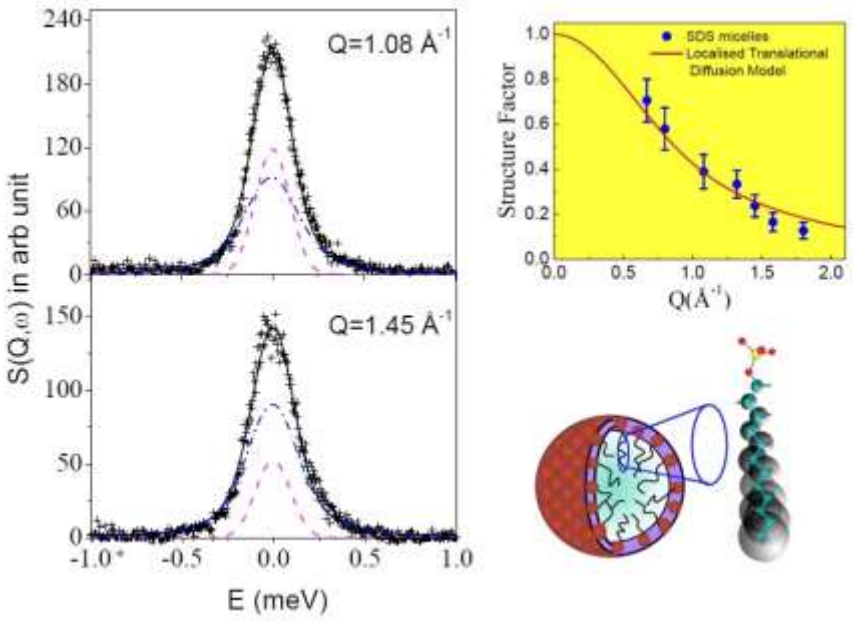

Fig. 11 Typical fitted QENS spectra for SDS micelles observed using MARX spectrometer at two different *Q* values (Left). Contribution of D_2O has been subtracted. Variation of EISF for SDS micelles with *Q* (Right). Solid line represents corresponds to localised translational diffusion model as depicted in the figure.

We have developed a model where hydrogen atoms undergo localized translational diffusion confined within spherical volumes, effectively captures the segmental dynamics of SDS molecules. This model describes the EISF well as shown in Fig. 11. Notably, this spherical volume and associated diffusivity expands linearly along the alkyl chain of SDS, as depicted in the schematic in the Fig 11. Consequently, hydrogen atoms closer to the head group diffuse within smaller spheres, exhibiting a lower diffusion constant than their counterparts away from the head group.

In-depth study of the micellar system continued through QENS experiments employing high-energy resolution spectrometers [77-82]. This exploration unveiled additional dynamical modes, including lateral diffusion of surfactants along the curved surface of micelles and rapid torsional motions, corroborated by our independent MD simulation studies [80]. Further insights into the dynamic landscape of self-assembled aggregates can be found in our recently published review article [83]. Additionally, our investigations explored into the impact of surfactant architecture, temperature variations, and the introduction of electrolytes on micellar dynamics. This comprehensive exploration has established correlations between dynamic behavior and microstructure, enhancing our understanding of the system's intricate properties.

4.5.2 Liposomes [84-106]

Liposomes are colloidal vesicles with concentric bilayers, wherein the aqueous compartment is completely enclosed by a bilayer membrane primarily composed of natural or synthetic lipids. Metallosome is a special class of liposome that are composed of metallosurfactants (MT) in which the polar headgroup of the surfactant molecule contains a metal centre as an integral structural component. Owing to the various functions derived from the metal centres together with their surface activity, MT can be potentially used in various applications including catalysts, medicines, and precursors for nanoparticles. These metallosomes are viable candidates for targeted drug delivery and the understanding of their membrane properties will be useful in enhancing their applicability. Particularly, the microscopic dynamics of lipids in the metallosomes can shed light on the drug release kinetics. QENS experiments were carried out using MARX spectrometer, Trombay on metallosomes formed by copper cetylpridinium chloride (Cu:CPC) MT to observe the effect of cholesterol on the membrane dynamics [84]. The experiments were carried out on Cu:CPC metallosomes with varying molar ratios of cholesterol at 1:0 and 1:0.5. Typical QENS spectra after D_2O subtraction for pure

metallosomes (1:0) is shown in Fig. 12 (a), along with the instrumental resolution of the spectrometer. Significant quasielastic broadening is observed over the instrumental resolution indicating presence of stochastic motions of the MT. Detailed data analysis suggests the presence of elastic component, indicating that the observed dynamics of MT is localised in nature. The typical fits for a QENS spectrum of metallosome at Q = 1.32 Å^{-1} is shown in the Fig. 12 (b) along with the individual elastic and quasielastic components. Elastic component refers to the contribution from the delta function and the quasielastic refers to contribution from the Lorentzian. The variation of the obtained EISF and HWHM for CuCPC metallosomes with and without cholesterol is shown with respect to the Q in Fig. 12 (c) and (d) respectively. Noteworthy is the observation that the EISF increases, and the HWHM decreases upon the addition of cholesterol. This suggests that the inclusion of cholesterol imposes constraints on the dynamics of metallosurfactants within the system, leading to an ordered membrane structure [84]. The findings from this study strongly suggest that the incorporation of cholesterol in metallosomes has a discernible impact on membrane dynamics. Consequently, this alteration holds the potential to significantly modulate the release kinetics of drugs targeted to specific sites within the system.

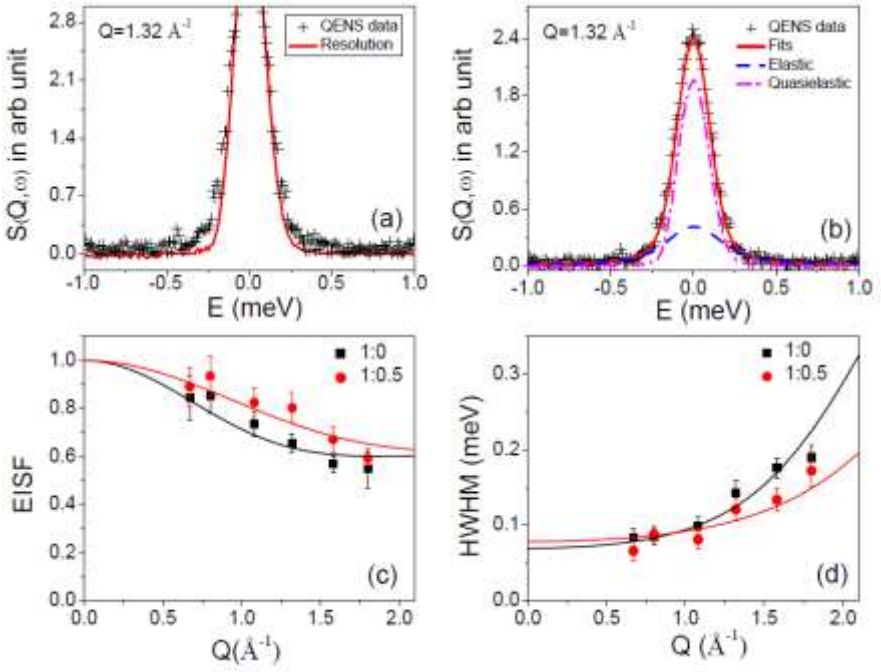

Fig. 12 (a) Illustration of the typical quasielastic broadening observed after D_2O subtraction for pure metallosomes over the instrument resolution as depicted by the solid line. (b) Typical fitted QENS spectrum of pure metallosomes using a sum of elastic and quasielastic components. The corresponding elastic and quasielastic components are explicitly displayed. Depiction of the variation of the (c) EISF and (d) HWHM with respect to Q for metallosomes, comparing samples with and without cholesterol. The solid lines indicate theoretical modeling based on the fractional localized translational diffusion model [84].

In addition to our exploration of metallosomes, our investigation extends to probing hierarchical dynamics in diverse vesicles systems [85-106]. Employing a range of QENS spectrometers with varying energy resolution and dynamic range, four distinct lipid motions: (i) long-range lateral, (ii) localized internal, (iii) collective bending, and (iv) thickness fluctuations were observed and described using suitable models. More details can be found in a recently published review article [106]. Furthermore, we have utilized this information on membrane dynamics to comprehend the interaction of various membrane-active molecules, including ionic liquids [91-96], nonsteroidal anti-inflammatory drugs (NSAIDs) [97-98], antimicrobial peptides [99], salts [100], curcumin [101], stimulants [102], and more, with lipid membranes.

5. Summary and Perspective

Quasielastic neutron scattering (QENS) is a powerful technique used to unravel the stochastic dynamics in condensed matter. The MARX spectrometer at Dhruva provides vital information in unraveling molecular dynamics across diverse condensed matter systems. Over several years, this state-of-the-art instrument has played a crucial role in examining the dynamics within molecular solids, liquid crystals, fluids confined in nanoscopic regimes (e.g., water filtration membranes, clays, zeolites), monolayer-protected nanosized metal clusters, self-assembled aggregates such as micelles and liposomes, and complex fluids like deep eutectic solvents and hydration gels. This comprehensive review showcases the extensive applications of QENS at Dhruva, leading to significant advancements in our understanding of diffusion mechanisms within condensed matter. These studies hold paramount importance for various domains within the Department of Atomic Energy (DAE), ranging from radioactive waste disposal to the exploration of energy materials and healthcare applications. In the context of radioactive waste disposal, the insights gained from QENS play a crucial role in optimizing storage and containment strategies, ensuring the safe and efficient management of nuclear waste. Additionally, in the realm of energy materials, understanding diffusion mechanisms aids in the design and development of advanced materials for nuclear reactors and energy storage applications. Moreover, the applications extend to healthcare, where the intricate dynamics revealed by QENS contribute to the advancement of drug delivery systems. By studying the diffusion of molecules in complex fluids and self-assembled structures, researchers can refine the design of pharmaceutical carriers, optimizing drug release kinetics for enhanced therapeutic outcomes. This interdisciplinary approach underscores the far-reaching impact of QENS research at Dhruva, not only in fundamental scientific understanding but also in addressing pressing challenges across diverse domains critical to the DAE multifaceted mission.

6. Acknowledgement

We sincerely acknowledge the contributions made by all of our collaborators. We also acknowledge Prof. R. Mukhopadhyay, who was primarily responsible for installing the MARX spectrometer.

References

1. W. Marshall and S.W. Lovesey, *Theory of Thermal Neutron Scattering* (Oxford: Clarendon Press, 1971)
2. M. Bée, *Quasielastic Neutron Scattering* (Bristol: Adam Hilger, 1988).
3. R. Hempelmann, *Quasielastic Neutron Scattering and Solid State Diffusion* (Oxford: Clarendon Press, 2000)
4. V. G. Sakai, C. A. Simionesco and S. H. Chen, *Dynamics of Soft Matter: Neutron Applications* (Springer: New York, 2012).
5. S. K. Agarwal, C.G. Karhadkar, A.K. Zope, Kanchhi Singh, *Nuclear Engineering and Design* **236** (2006) 747–757
6. R. Mukhopadhyay, S. Mitra, S. K. Paranjpe, B. A. Dasannacharya, *Nucl. Instrum. Methods Phys. Res., Sect. A* **474** (2001) 55.
7. S. Mitra, Binoj Nair, T. Pradeep, P.S. Goyal, R. Mukhopadhyay, *J. Phys. Chem. B* **106** (2002) 3960
8. T. Pradeep, S. Mitra, A. Sreekumaran Nair, and R. Mukhopadhyay, *J. Phys. Chem. B* **108** (2004) 7012
9. R. Mukhopadhyay, S. Mitra, I. Tsukushi, S. Ikeda, T. Pradeep, *Chemical Physics* **292** (2003) 223–227
10. R. Mukhopadhyay, S. Mitra, T. Pradeep, I. Tsukushi, S. Ikeda, *J. Chem. Phys.* **118** (2003) 4614
11. S. Mitra, V. K. Sharma, T. Pradeep, M. Johnson and R.Mukhopadhyay, *AIP Conf. Proc*., **1313** (2010) 292-294
12. R. Mukhopadhyay, S. Mitra, M. Johnson, V. R. Rajeev Kumar and T. Pradeep, *Phys. Rev. B* **75** (2007) 075414

13 S. Gautam, R.R. Choudhury, Lata Panicker, S. Mitra, R. Mukhopadhyay, *Chemical Physics Letters* **453** (2008) 207–211
14. S. Mitra, V.S.S. Sastry, K. Venu, R. Mukhopadhyay, *Chemical Physics Letters* **406** (2005) 263–267
15. S. Gautam, R.R. Choudhury, Lata Panicker, S Mitra and R. Mukhopadhyay, *Pramana J. Phys.***71** (2008) 1159-1164
16. S. Mitra, R. Mukhopadhyay, K. Venu, *Chemical Physics* **261** (2000) 149-156
17. A.J. Leadbetter, M.A. Mazid, B.A. Kelly, J.W. Goodby, G.W. Gray, *Phys. Rev. Lett.* **43** (1979) 630.
18. S. Mitra, V. K. Sharma and R. Mukhopadhyay, *Rep. Prog. Phys.* **84** (2021) 066501
19. V. K. Sharma, S. Mitra and R. Mukhopadhyay, J. *Phys. Soc. Japan* **82** (2013) SA006
20. S. Mitra, V. K. Sharma, R. Mukhopadhyay, *Neutron News* **25** (2014) 38
21. V. K. Sharma, S. Gautam, S. Mitra and R. Mukhopadhyay, *Z. Phys. Chem.* **224** (2010) 133
22. V. K. Sharma, P.S. Singh, S. Gautam, P. Maheshwari, D. Dutta and R. Mukhopadhyay, *J. Memb. Sci.* **326** (2009) 667
23. V. K. Sharma, P. S. Singh, S. Gautam, S. Mitra and R. Mukhopadhyay, *Chem. Phys. Lett.* **478** (2009) 56
24. V. K. Sharma, S. Mitra, P. Singh, F. Jurany, and R. Mukhopadhyay, *Euro. Phys. J. ST* **189** (2010) 217
25. V. K. Sharma, H. Srinivasan, Priya Maheshwari, S. Mitra and P. K. Pujari, Distinct Regimes of Nanoconfined Water in the Pores: A Quasi-elastic Neutron Scattering and Positron Annihilation Spectroscopic Study (to be submitted)
26. D. Chakrabarty, Siddharth Gautam, S. Mitra, Antonio Gil, Miguel A. Vicente, R. Mukhopadhyay, *Chem. Phys. Lett.* **426** (2006) 296
27. S.A. Prabhudesai,V. K. Sharma, D. Chakrabarty, Miguel A. Vicente, S. Mitra and R. Mukhopadhyay, *AIP Conf. Proc.* **1349** (2011) 1001.
28. S. A. Prabhudesai, V. K. Sharma, S. Mitra, D. Chakrabarty, M. A. Vicente, J. Peter Embs and R. Mukhopadhyay, *J. Phys. Soc. Japan* **82** (2013) SA009
29. S. Mitra, S.A. Prabhudesai, V.K. Sharma, P. Maheshwari, D. Chakrabarty, M.A. Vicente, J. Peter Embs and R. Mukhopadhyay, *AIP Conf. Proc.* **1447** (2012) 935
30. S. Mitra, S. A. Prabhudesai, D Chakraborty, V. K. Sharma, M. Vicente, J.P. Embs and R. Mukhopadhyay, *Phys. Rev. E* **87** (2013) 062317
31. R. R. Dessai, V. K. Sharma, S. A. Prabhudesai, S. Mitra, J. A. E. Desa and R. Mukhopadhyay, *J. Phys. Soc. Japan* **82** (2013) SA008
32. S. Mitra, A. Pramanik, D. Chakrabarty and R. Mukhopadhyay, *Pramana J. Phys.* **63** (2004) 437
33. S. Mitra, A Pramanik, D Chakrabarty, F Jurányi, S Gautam and R Mukhopadhyay, *Journal of Physics: Conference Series* **92** (2007) 012167
34. V. K. Sharma, S. Mitra, A. Kumar, S. M. Yusuf, F. Juranyi and R. Mukhopadhyay, *J. Phys. Cond. Mat.* **23** (2011) 446002
35. V. K. Sharma, S. Mitra, N. Thakur, S. M. Yusuf, Fanni Juranyi and R. Mukhopadhyay, *J. Appl. Phys.* **116** (2014) 034909
36. S. Mitra, V.K. Sharma, N. Thakur, S.M. Yusuf, F. Juranyi and R. Mukhopadhyay, *EPJ Web of Conf.* **83** (2015) 02012
37. S Mitra, R Mukhopadhyay, I Tsukushi, S Ikeda, *Journal of Physics: Condensed Matter* **13** (2001), 8455
38. R Mukhopadhyay, S Mitra, KT Pillai, I Tsukushi, S Ikeda, *Applied Physics A* **74** (2002) s1314-s1316
39. S Mitra, R Mukhopadhyay, KS Chandrasekaran, *Physica B* **292** (2000), 29-34
40. S. Mitra, R. Mukhopadhyay, *Current Science* **84** (2003) 653
41. M. Alborzfar, G. Jonsson, C. Grøn, *Wat. Res*. **32** (1998) 2983.
42. V. K. Sharma, S. Gautam, S. Mitra, Mala N. Rao, A. K. Tripathi, S. L. Chaplot and R. Mukhopadhyay, J. *Phys. Chem. B* **113** (2009) 8066
43. S. Mitra, V.K. Sharma, S.L. Chaplot, R. Mukhopadhyay, *Chem. Phys.* **430** (2014) 69

44. S. Mitra, V. K. Sharma and R. Mukhopadhyay, *AIP Conf. Proc.* **1349** (2011) 54
45. V. K. Sharma, Mala N. Rao, S. Gautam, A. K. Tripathi, V. S. Kamble, S. L. Chaplot and R. Mukhopadhyay, *Pramana-J. Phys.* **71** (2008) 1165
46. Siddharth Gautam, V.K. Sharma, S. Mitra, S.L. Chaplot and R. Mukhopadhyay, *Chem. Phys. Lett.* **501** (2011) 345.
47. R. Mukhopadhyay, A. Sayeed, S. Mitra, A.V. Anil Kumar, Mala N. Rao, S.L. Chaplot and S. Yashonath, *Phys. Rev. E* **66** (2002) 061201
48. S. Mitra, R. Mukhopadhyay, A. Sayeed, S. Yashonath and S.L. Chaplot, *Applied Physics A* **74** (2002) S1317
49. A. Sayeed, S. Mitra, A.V. Anil Kumar, R. Mukhopadhyay, S. Yashonath and S.L. Chaplot, *J. Phys. Chem. B* **107** (2003) 527
50. R. Mukhopadhayay, A. Sayeed, Mala N. Rao, A.V. AnilKumar, S. Mitra, S. Yashonath and S.L. Chaplot, *Chem. Phys.* **292** (2003) 217
51. S. Mitra, S. Sumitra, A.M. Umarji, R. Mukhopadhyay, S. Yashonath and S.L. Chaplot, *Pramana J. Phys.* **63** (2004) 449
52. S. Gautam, S. Mitra, R. Mukhopadhyay, and S. L. Chaplot, *Phys. Rev. E* **74** (2006) 041202.
53. S. Mitra, S. Gautam, R. Mukhopadhyay, S. Sumitra, A.M. Umarji, S. Yashonath, S.L. Chaplot, *Physica B* **385–386** (2006) 275
54. S. Gautam, S. Mitra, A. Sayeed, S. Yashonath, S.L. Chaplot, R. Mukhopadhyay, *Chem. Phys. Lett*. **442** (2007) 311
55. S. Gautam, S. Mitra, S. L. Chaplot, and R. Mukhopadhyay, *Phys. Rev. E* **77** (2008) 061201
56.S. Gautam, S Mitra and R Mukhopadhyay, *Pramana J. Phys.* **71** (2008) 809
57. S. Gautam, A K Tripathi, V S Kamble, S Mitra and R Mukhopadhyay, *Pramana J. Phys.* **71** (2008) 1153.
58. A.K. Tripathi, A. Sahasrabudhe, S. Mitra, R. Mukhopadhyay and N.M. Gupta, *Phys. Chem. Chem. Phys*. **3** (2001) 4449
59. A. Sahasrabudhe, S. Mitra, A. K. Tripathi, R. Mukhopadhyay and N.M. Gupta, *J. Phys. Chem. B* **106** (2002) 10923
60. S. Mitra, R. Mukhopadhyay, A.K. Tripathi and N.M. Gupta, *Applied Physics A* **74** (2002) S1308
61. A. Sahasrabudhe, S. Mitra, A. K. Tripathi, R. Mukhopadhyay and N.M. Gupta, *Phys. Chem. Chem. Phys.* **5** (2003) 3066
62. S. Mitra, V.S. Kamble, A. K. Tripathi, N.M. Gupta and R. Mukhopadhyay, *Pramana J. Phys.* **63** (2004) 443
63. N.M. Gupta, Dharmesh Kumar, V.S. Kamble, S. Mitra, R. Mukhopadhyay and V.B. Kartha, *J. Phys. Chem. B* **110** (2006) 4815.
64. V. K. Sharma, S. Mitra, S.L. Chaplot and R. Mukhopadhyay, *AIP Conf. Proc.* **1313** (2010) 325
65. V. K. Sharma, S. Mitra, P. Maheshwari, D. Dutta, P. K. Pujari, and R. Mukhopadhyay, *Euro. Phys. J. ST* **189** (2010) 273
66. D. R. Cole, E. Mamontov, G. Rother, Chapter 19, In Neutron Applications in Earth, Energy and Environmental Sciences; Eds. L. Liang,. R. Rinaldi,. H. Schober, Springer-Verlag: Berlin, 2009.
67 H. Srinivasan, V. K. Sharma, and S. Mitra, *PCCP* **23** (2021) 22854 - 22873
68 H. Srinivasan, P. S. Dubey, V. K. Sharma, R. Biswas, S. Mitra and R. Mukhopadhyay, *AIP Conf. Proc.* **1942** (2018) 110032
69 H. Srinivasan, V. K. Sharma, S. Mitra, R. Biswas, R. Mukhopadhyay, *Physica B* **562**, (2019) 13
70 H. Srinivasan, V. K. Sharma, S. Mitra, J. Phys. Chem B **126** (2022) 9026.
71 H. Srinivasan, V. K. Sharma, and S. Mitra, *J. Chem. Phys.* **155** (2021) 024505
72 H. Srinivasan, V. K. Sharma, V. G. Sakai, R. Mukhopadhyay, and S. Mitra, *J. Phys. Chem. Lett.* **14** (2023) 9766.
73. P. Biswas, S. Chaitanya, R. Johnson, S. Prabhudesai, V. K. Sharma, S. Mitra and R. Mukhopadhayay, *Open Journal of Inorganic Chemistry* **3** (2013) 48
74. K. Rajeswari, Papiya Biswas, Roy Johnson, S. Prabhudesai, V. K. Sharma, S. Mitra and R. Mukhopadhayay, *J. Disp. Sc. Tech* **35** (2014) 1442

75 P. S. Dubey, Mathias B. Lawrence, H. Srinivasan, V. K. Sharma*, and S. Mitra, AIP *Conf. Proc.* **2115** (2019) 030040
76. V. K. Sharma, G. Verma, S. Gautam, P. A. Hassan, S. Mitra and R. Mukhopadhyay, *Phys. Chem.* **224** (2010) 253
77. V. K. Sharma, S. Mitra, G. Verma, P. A. Hassan, V. Garcia Sakai and R. Mukhopadhyay, *J. Phys. Chem. B* **114** (2010) 17049
78. V. K. Sharma, S. Mitra, V. Garcia Sakai and R. Mukhopadhyay, *J. Phys. Chem. B* **116** (2012) 9007
79. V. K. Sharma, S. Mitra, M. Johnson and R. Mukhopadhyay, *J. Phys. Chem. B* **117** (2013) 6250
80. B. Aoun, V. K. Sharma, E. Pellegrini, S. Mitra, M. Johnson, and R. Mukhopadhyay *J. Phys. Chem. B* **119** (2015) 5079
81. V. K. Sharma, H. Srinivasan, S. Mitra, V. Garcia-Sakai, R. Mukhopadhyay, *J. Phys. Chem. B* **121** (2017) 5562
82. V. K. Sharma, H. Srinivasan, R. Mukhopadhyay, V. Garcia Sakai and S. Mitra, *J. Mol. Liquids* **332** (2021) 115722
83. V. K. Sharma, S. Mitra, R. Mukhopadhyay, *Langmuir* **35** (2019) 14151
84. B. Kaur, G. Kaur, G. R. Chaudhary, V. K. Sharma, H. Srinivasan, S. Mitra, A. Sharma, Santosh L. Gawali, P.A. Hassan, *J. Mol. Liquids* **318** (2020) 114034
85. S. Mitra, V. K. Sharma, V. Garcia-Sakai, A. Orecchini, T. Seydel, M. Johnson and R Mukhopadhyay, *J. Phys. Chem. B* **120** (2016) 3777
86. P. S. Dubey, H. Srinivasan, V. K. Sharma, S. Mitra, V. Garcia Sakai and R. Mukhopadhyay, *Scientific Reports* **8** (2018) 1862
87 H. Srinivasan, V. K. Sharma, S. Mitra, and R. Mukhopadhyay, *J. Phys. Chem. C* **122** (2018) 20419
88. H. Srinivasan, V. K. Sharma, S. Mitra, V. G. Sakai, R. Mukhopadhyay, *Physica B* **562** (2019) 55
89.V. K. Sharma, H. Srinivasan, V. García Sakai, S. Mitra, *Struct Dyn.* **7** (2020) 051301
90. J. Gupta, V. K. Sharma, H. Srinivasan, H. Bhatt, S. Kumar, M. Sarter, V. G. Sakai, S. Mitra, *Phys. Rev. Mat.* **6** (2022) 075602.
91. J. Gupta, V. K. Sharma, H. Srinivasan, H. Bhatt, V. G. Sakai, R. Mukhopadhyay, Langmuir (2023) DOI: 10.1021/acs.langmuir.3c02755.
92.V. K. Sharma, S. K. Ghosh, P. Mandal, T. Yamada, K. Shibata, S. Mitra and R. Mukhopadhyay, *Soft Matter* **13** (2017) 8969
93. V. K. Sharma, S. K. Ghosh, V. García Sakai and R. Mukhopadhyay, *Front. in Chem.* **8** (2020) 1004
94. K. Bakshi, S. Mitra, V. K. Sharma, M. S. K. Jayadev, V. Garcia Sakai, R. Mukhopadhyay, A. Gupta, S. K. Ghosh, *BBA-Biomembrane* **1862** (2020) 183103
95. S. Mitra, V. K. Sharma, S. K. Ghosh, *Chem. Phys. Lipids* **256** (2023) 105336
96. V. K. Sharma and R. Mukhopadhyay, *Biophysical Reviews* **10** (2018) 721
97. P. S. Dubey, V. K. Sharma, H. Srinivasan, S. Mitra, V. García Sakai and R. Mukhopadhyay, *J. Phys. Chem. B* **122** (2018) 9962
98. S. Sahu, H. Srinivasan, S. E. Jadhav, V. K. Sharma, A. Debnath, *Langmuir* **39** (2023) 16432
99. J. B. Mitra, V. K. Sharma, A. Mukherjee, V. Garcia Sakai, A. Dash, and M. Kumar, *Langmuir* **36** (2020) 397
100. V. K. Sharma, J. Gupta and E. Mamontov, *Soft Matter* 19 (2023) 57.
101. V. K. Sharma, J. Gupta, H. Srinivasan, H. Bhatt, V. G. Sakai and S. Mitra, *Langmuir* **38** (2022) 9649–9659
102. V. K. Sharma, H. Srinivasan, V. García Sakai, and S. Mitra, *J. App. Phys.* **128** (2020) 154701
103. P. Singh, V. K. Sharma, S. Singha, V. G. Sakai, R. Mukhopadhyay, R. Das and S. K. Pal, *Langmuir* **35** (2019) 4682
104. V. K. Sharma, H. Srinivasan and S. Mitra, *AIP Conf. Proc.* **2265** (2020) 20001
105.S. Qian, V. K. Sharma, L. A. Clifton, *Langmuir* **36** (2020) 15189−15211
106. V. K. Sharma, E. Mamontov, *Progress in Lipid Research* **87** (2022) 101179

Neutron Conferences and Workshops

January 2024

Workshop - The 2nd Winter School of SANS Data Analysis at SNS
January 8-11, 2024, Oak Ridge, TN, USA
https://conference.sns.gov/event/401/

Future Perspectives on Neutron Scattering
January 17, 2024, London, UK
https://iop.eventsair.com/fpns2024/

2nd French-Swiss Meeting SANS for Soft Matter
January 24-25, 2024 , PSI, Villigen, Switzerland
https://indico.psi.ch/event/14807/

February 2024

XXth School on Neutrons as Probes of Condensed Matter
February 05-10, 2024, BARC, Mumbai, India
https://www.csr.res.in/news/NPCM-2024-Announcement-POSTER.pdf

Workshop on Scientific Benefits and Applications of Resonant Spin Echo
February 13-15, 2024, Oak Ridge, TN, USA
https://conference.sns.gov/event/393/

Workshop - HERCULES European School-Neutrons & Synchrotron Radiation for Science
February 26- March 28 2024, Grenoble, France
https://hercules-school.eu/

March 2024

Workshop - French-Swedish Advanced School on Structural X-Ray and Neutron Scattering Techniques
March 11-15, 2024, Lund, Sweden
https://indico.esss.lu.se/event/3378/

April 2024

Conference - Machine Learning Conference for X-Ray and Neutron-Based Experiments
April 8-10, 2024, Heinz Maier-Leibnitz Zentrum (MLZ), Garching, Munich Germany
https://indico.frm2.tum.de/event/451/

June 2024

Conference - 12th World Conference on Neutron Radiography
June 2-7, 2024, Idaho Falls, ID, USA
https://inl.gov/events/12th-world-conference-on-neutron-radiography/

Conference - MLZ Conference 2024 on Neutrons for Energy Storage
June 4-7, 2024, Munich, Germany
https://indico.frm2.tum.de/event/461/

Workshop – 16th Bombannes Summer School: Scattering Methods Applied to Soft Condensed Matter
June 4-11, 2024, Bombannes/Carcans-Maubuisson, France
https://www-llb.cea.fr/Phocea/Vie_des_labos/Seminaires/index.php?id=4626

Conference - Neutrons in Structural Biology – Challenges and Opportunities
June 10-12, 2024, Oak Ridge, TN, USA
https://conference.sns.gov/event/402/

Conference – Quasi elastic neutron scattering (QENS) and workshop on Inelastic neutron spectrometers (WINS) 2024
June 10-14, 2024, Manchester, UK
https://iop.eventsair.com/qens-wins2024

Conference - Neutrons & Food 7
June 10-14, 2024
STAR Tower, University of Delaware, Newark, United States
https://sites.udel.edu/neutronsandfood7/

Seminar - Bridging Length Scales in Magnetism – Diffuse Scattering from the Atomic to the Mesoscale
June 17-20, 2024, Bad Honnef, Germany
https://www.we-heraeus-stiftung.de/english/

American Conference on Neutron Scattering (ACNS 2024)
June 23-27, 2024, Knoxville, TN, USA
https://ceramics.org/event/american-conference-on-neutron-scattering-acns-2024/

July 2024

Conference - SXNS17: 17th International Surface X-ray and Neutron Scattering Conference
July 15-18, 2024, Grenoble, France
https://www.ill.eu/news-press-events/events-calendar

August 2024

International Conference on Neutron Physics and Neutron Scattering
August 05-06, 2024 in Montreal, Canada
https://waset.org/neutron-physics-and-neutron-scattering-conference-in-august-2024-in-montreal

September 2024

International Conference on Neutron Physics and Neutron Scattering
September 20-21, 2024, Lisbon, Portugal
https://waset.org/neutron-physics-and-neutron-scattering-conference-in-september-2024-in-lisbon

November 2024

Conference - The XIX edition of the International Small-Angle Scattering Conference
3-8 November 2024, Taipei, Taiwan
https://www.sas2024.tw/site/page.aspx?pid=901&sid=1535&lang=en

AONSA Neutron School 2024
3-8 November 2024, BARC, Mumbai, India
https//aonsa.org/neutron_schools/

Neutron Scattering Society of India

(Registered No. Maharashtra State, Mumbai, 2011 GBBSD/1696)

(For Promotion of Neutron Scattering Research in India)

C/o Solid State Physics Division,
Bhabha Atomic Research Centre, Mumbai 400085

Phones: 91-22-25595376, 25593757, 25594930

Email:neutron@barc.gov.in; URL: http://www.**nssi.org.in**

Affix your PP size recent photograph here

Application Form for Membership*

Name (in Capital letters)$: Prof/Dr/Ms/Mr (Surname last)	
Nationality:	**Date of Birth:** (dd/mm/yyyy)
Academic Qualification:	**Sex: M/F**
Profession:	**Neutron User Experience** (in yrs):
Nature of Present work:	
Affiliation: **Pin Code:**	**Residential Address:** **Pin Code:**
STD Code & Phone (O):	**STD Code & Phone (R):**
STD Code & FAX No.	**Mobile:**
Email-1:	**Email-2:**
+Details of Cheque/DD+: No.	**dated** **Bank:**
Endorsed by: (Either an existing member of NSSI or Head of the Affiliated Institute/University) **Name & Designation** **Signature**	
Date:	**Signature:**

*Life Membership fee: Rs. 1000/- (One thousand only),
Details for Online Payment:
Account Name: NEUTRON SCATTERING SOCIETY OF INDIA
Bank Name: STATE BANK OF INDIA, BARC BRANCH, MUMBAI 400085, INDIA
Account No.: 034237290776
IFSC Code: SBIN0001268

To: Secretary, ***Neutron Scattering Society of India***